
SKewed NEURONAL HETEROGENEITY ENHANCES EFFICIENCY ON VARIOUS COMPUTING SYSTEMS

Arash Golmohammadi

arash.golmohammadi@med.uni-goettingen.de

Jannik Luboeinski

jannik.luboeinski@med.uni-goettingen.de

Christian Tetzlaff

christian.tetzlaff@med.uni-goettingen.de

Group of Computational Synaptic Physiology, Department for Neuro- and Sensory Physiology,
University Medical Center Göttingen, Humboldtallee 23, 37073 Göttingen, Germany

Campus Institute Data Science (CIDAS), Goldschmidtstraße 1, 37077 Göttingen, Germany

ABSTRACT

Heterogeneity is a ubiquitous property of many biological systems and has profound implications for computation. While it is conceivable to optimize neuronal and synaptic heterogeneity for a specific task, such top-down optimization is biologically implausible, prone to catastrophic forgetting, and both data- and energy-intensive. In contrast, biological organisms, with remarkable capacity to perform numerous tasks with minimal metabolic cost, exhibit a heterogeneity that is inherent, stable during adulthood, and task-unspecific. Inspired by this intrinsic form of heterogeneity, we investigate the utility of variations in neuronal time constants for solving hundreds of distinct temporal tasks of varying complexity. Our results show that intrinsic heterogeneity significantly enhances performance and robustness in an implementation-independent manner, indicating its usefulness for both (rate-based) machine learning and (spike-coded) neuromorphic applications. Importantly, only skewed heterogeneity profiles—reminiscent of those found in biology—produce such performance gains. We further demonstrate that this computational advantage eliminates the need for large networks, allowing comparable performance with substantially lower operational, metabolic, and energetic costs, respectively *in silico*, *in vivo*, and on neuromorphic hardware. Finally, we discuss the implications of intrinsic (rather than task-induced) heterogeneity for the design of efficient artificial systems, particularly novel neuromorphic devices that exhibit similar device-to-device variability.

1 Introduction

The brain is a complex recurrent neural network (RNN) whose dynamics—the temporal activity of its constituent neurons—underlie thoughts, behaviors, and actions. Neuronal activity depends strongly on the electrophysiological properties of neurons and synapses. These properties, alongside the anatomical connectivity, enable the brain to execute a plethora of cognitive tasks with an estimated power consumption of only 20 W [1]. Therefore, understanding the structure within these properties allows us to design more capable and efficient artificial systems.

Unlike electronic or artificial systems, in which units are designed to be identical, biological neurons and synapses exhibit a large electrophysiological heterogeneity [2–11], sometimes exceeding two orders of magnitude within the same neuronal type. Focusing on specific tasks, several theoretical [12–25] and experimental studies [26–30] have demonstrated the computational benefits of such heterogeneities. Consequently, heterogeneous parameter organization is not an imperfection; rather, it is a feature that the brain actively exploits.

Neuronal heterogeneity can be organized either top-down, in a task-informed manner, or bottom-up, intrinsically and task-agnostically. In the former case, each heterogeneous property is treated as a degree of freedom that is optimized for high-level objective function(s). This approach—the mainstream paradigm in machine learning—has proven remarkably effective. In particular, gradient-based learning combined with neuronal heterogeneity achieves perfor-

mance equal to or better than the state of the art on several common benchmarks [31–35]. Despite this success, the error-backpropagation rule is criticized for its biological implausibility [36, 37], its task-specificity, and the resulting catastrophic-forgetting phenomenon [38, 39]. While strategies have been proposed to mitigate these problems at the synaptic level [37, 39], they fall short at the neuronal level. A top-down optimization of neuronal heterogeneity would require drastic activity-dependent changes in either the neurons’ passive biophysical properties or their morphology—yet both are known to remain largely stable throughout adulthood in mammals [40, 41]. Moreover, end-to-end training of large artificial models, even for a single task, is energetically costly [42] and data-intensive [43, 44].

In contrast, intrinsic parameter heterogeneity does not suffer from the issues of task-specificity and high computational cost. Hence, it is reasonable to assume that biological properties are organized intrinsically. However, it is not immediately clear whether such a task-agnostic parameter organization can support the vital and cognitive computations required by living organisms.

We address this question by constructing rate- and spiking-based RNNs with varying levels of intrinsic neural heterogeneity and evaluating their performance on hundreds of dissimilar tasks that span a wide spectrum of complexities. To measure the innate computational capacity of the networks, we adopt the reservoir-computing paradigm [45–47], which means that we train a linear readout for each task and quantify its generalization score. The rate-based networks serve as prototypes for common machine-learning models, allowing us to assess the general effect of task-unspecific heterogeneity. In contrast, the spiking networks illustrate how these effects translate to a more biologically realistic, event-based coding scheme. Our approach thus combines the work of [33] and [48], who considered only spike- or rate-based RNNs, while substantially expanding the task space. Additionally, by emulating our spiking networks on two neuromorphic platforms and measuring their energy consumption, we demonstrate that novel computing systems also benefit from intrinsic heterogeneity. In particular, this work substantially revises and extends our previous preprint [49].

Our results indicate that a specific form of intrinsic heterogeneity significantly enhances both overall performance and robustness, and it does so irrespective of the neural code—whether rate- or spike-based. In particular, we observe that small, heterogeneous RNNs substantially outperform larger homogeneous networks, yielding simpler systems with higher energy efficiency. We show that the computational principle underlying this performance boost is *resource diversification*, which serves as an inductive bias [50], facilitating the execution of diverse tasks across various computing systems.

2 Results

2.1 Networks setup

We construct several recurrent neural networks that differ only in the distribution of their neuronal membrane-time constants (Fig. 1A). All networks receive a time-dependent, multidimensional chaotic input $u(t)$ that emulates the multimodal, partially predictable nature of sensory stimuli in the brain. In addition, each neuron is driven by i.i.d. white noise (Fig. 1B). Neurons evolve according to either rate-based (leaky integrator, LI) or spike-based (leaky integrate-and-fire, LIF) dynamics. As in the standard reservoir-computing paradigm, network performance is assessed by quantifying the mismatch between a ground-truth target function $y(t)$ and the best linear reconstruction of that target from the neuronal state $X(t)$ (Fig. 1C, E, and F). Specifically, we use the coefficient of determination as our performance metric, where a value of 1 indicates perfect performance, 0 indicates chance-level performance, and values below 0 indicate worse-than-chance performance.

Unless otherwise stated, membrane time constants are drawn from a log-normal distribution with mean $\mathbb{E}[\tau]$ and variance level $\text{Var}[\tau] = h \cdot \mathbb{E}[\tau]^2$ with $h \in \{0, 0.1, 1, 10\}$ quantifying different levels of heterogeneity. To emulate the multimodal, partially predictable nature sensory inputs in the brain, we employed a multidimensional chaotic time series. The input $u(t)$ is generated from the trajectory of various systems, such as the chaotic Lorenz system [51] or the Mackey-Glass. In the following we will discuss results for the Lorenz system as example. Please see the Supplementary Material for other input systems. The remaining hyper-parameters are: network size $N = 250$, connection probability $p = 0.1$, excitatory/inhibitory ratio $f = N_E/N_I = 4$, weight dispersion $\sigma_0 = 1$, recurrent gain $J = 1$, feedforward gain $J_u = 1$, noise intensity $J_n = 0.1$ (corresponding to a signal-to-noise ratio of 10), and mean of membrane time distributions $\mathbb{E}[\tau] = 1$. All of these hyper-parameters are varied in Section 2.4 to assess the robustness of our findings to these choices.

2.2 Tasks desiderata and the benchmark quality check

To evaluate the computational capacity of each network in a task-independent way, we test it on a large set of *dissimilar* tasks that span a broad range of complexities. If the tasks were all too easy (or all too difficult), every net-

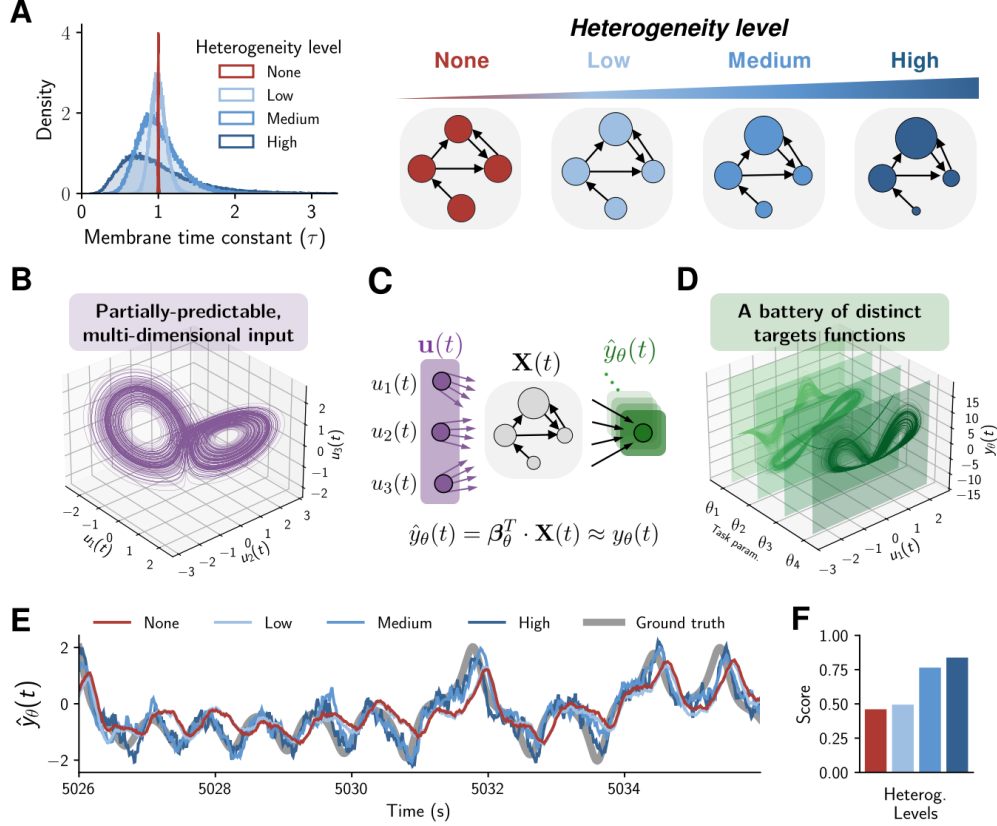


Figure 1: Method summary. (A) Schematic of heterogeneous networks. (Left) Membrane time constants of neurons are drawn from a log-normal distribution with a fixed mean; the variance controls the level of heterogeneity. (Right) Apart from the neuronal time constants (values are indicated by different radii), the networks have identical connectivity and inputs. (B) A multi-dimensional chaotic time series \mathbf{u} , mimicking partially predictable multi-modal sensory stimuli, drives the network dynamics. In addition, each neuron receives white noise with 10% of the stimulus variance (not shown). (C) Schematic of the reservoir computing paradigm. The network’s state $\mathbf{X}(t)$ is used to reconstruct a set of target functions $y_\theta(t)$ via the optimal task-specific linear readout β_θ . (D) Tasks belong to a family \mathcal{F}_θ , parameterized by $\theta = (\Delta, d, k)$, which captures working-memory-like computations such as memory recall, forecasting, and nonlinear processing by transforming the stimulus $\mathbf{u}(t)$. (E) Network outputs, $\hat{y}_\theta(t) = \beta_\theta^T \cdot \mathbf{X}(t)$, for an exemplary task. Colors indicate different heterogeneity levels as in (A). The ground-truth $y_\theta(t)$ (thick gray line) is shown for comparison. (F) Performance associated with the traces shown in (E). Performance of each network is measured by the coefficient of determination, a scalar score that quantifies the normalized mismatch between the ground truth and the output over an unobserved test interval. A value of 1 indicates a perfect match, while 0 corresponds to chance-level performance. Colors as in (E).

work—regardless of its level of heterogeneity—would either succeed or fail uniformly, providing little insight into how heterogeneity influences performance. By using a benchmark that includes a range of task complexities, we obtain a more informative measure of the computational impact of intrinsic heterogeneity.

The space of all possible tasks is infinite, so one must inevitably focus on a single class of tasks. Here we concentrate on the generic form of tasks, defined as a mapping \mathcal{F} from the time-dependent input $\mathbf{u}(t)$ to the target output $y(t)$. This mapping can be chosen arbitrarily. What distinguishes it from other classes of tasks is that the output $y(t)$ is purely a function of the input $\mathbf{u}(t)$ and, importantly, is independent of the network’s internal state $\mathbf{X}(t)$. Note that many cognitive working-memory tasks can be cast in this form. For convenience, we use a parameterized mapping $\mathcal{F}_\theta(\cdot)$ with the functional form $\mathcal{F}_\theta(\mathbf{u}(t)) = u_k(t + \Delta)^d$, where $\theta = (k, \Delta, d)$ are the mapping parameters. The shift Δ moves the input forward or backward in time emulating memory recall or stimulus forecasting, the exponent $d \in \mathbb{N}$ controls the degree of nonlinearity applied to the time-shifted stimulus mirroring nonlinear input processing, and the index $k \in \{1, \dots, K\}$ selects which input modality is extracted or attended. Some exemplary traces are shown in Fig. 1D. Using the parameter ranges $k \in \{1, 2, 3\}$, $d \in \{1, 2, \dots, 6\}$, and $\Delta \in [-2, 2]$, we uniformly sampled a set of 882 tasks from the \mathcal{F}_θ mapping. The extent of mutual independence and the complexity of these tasks were then examined, respectively via the cosine similarity between each pair of tasks and the cosine dissimilarity between each

task and a reference task. We used the identity task ($y(t) = u_k(t)$) as our reference, since this task merely relays the k -th component of the input and requires no memory or nonlinear processing. As Fig. 2A shows, the majority of the tasks are independent of one another. Moreover, Fig. 2B illustrates a broad spectrum of task complexities. This wide spectrum is, to a great extent, inherited from the unpredictability of chaotic time series, which even without mapping, serve as an ideal benchmark for time series modeling [52]. Together with the sheer number of tasks, this evidence attests to the high quality of our curated benchmark. In what follows, we discuss how different heterogeneity levels alter the “performance profile” of RNNs for this comprehensive, low-bias benchmark.

2.3 Heterogeneity increases performance score across tasks

Using our benchmark, we compared the performance scores of heterogeneous and homogeneous RNNs on each task. The panels in Fig. 2C show the performance profile for a representative subset of tasks that probe the network’s (quadratic) memory or prediction capabilities ($k = 1, d = 2$, with various temporal-shift values Δ). In both rate- and spike-based implementations, increasing heterogeneity yields higher performance scores across almost the entire range of Δ . The small score standard deviation (even after 10-fold enlargement) indicates that this improvement is statistically significant (see Section 2.4). Importantly, this improvement is not confined to this particular subset. As the panels in Fig. 2D illustrate, in both implementations the scores of heterogeneous networks (plotted on the y-axis) are systematically greater than those of the corresponding homogeneous networks (plotted on the x-axis) for the same task.

To verify that the performance boost does not depend on the stimulus structure, we replaced the Lorenz input with a three-dimensional signal whose components were generated from three independent one-dimensional Mackey–Glass time series (two of them chaotic). As Fig. S.3 shows, unlike the Lorenz input, this multidimensional stimulus lacks any topological structure and therefore generally yields a more difficult collection of tasks (compare Fig. S.4B with Fig. 2B). Nevertheless, as shown in Figs. S.4C–D, heterogeneous networks still outperform homogeneous ones in both rate- and spike-based implementations. See also Figs. S.5 and S.6 for stimuli with higher and lower predictability, respectively.

2.4 Heterogeneous networks are more robust to hyperparameters variation

To assess whether the performance gains induced by heterogeneity depend on the RNN hyperparameters, we systematically varied several key settings and recomputed the performance profiles of the networks as described above. For brevity, we report only the changes in mean performance here; the full distributions of scores across individual tasks, together with their uncertainties, are provided in Sections F and G, respectively.

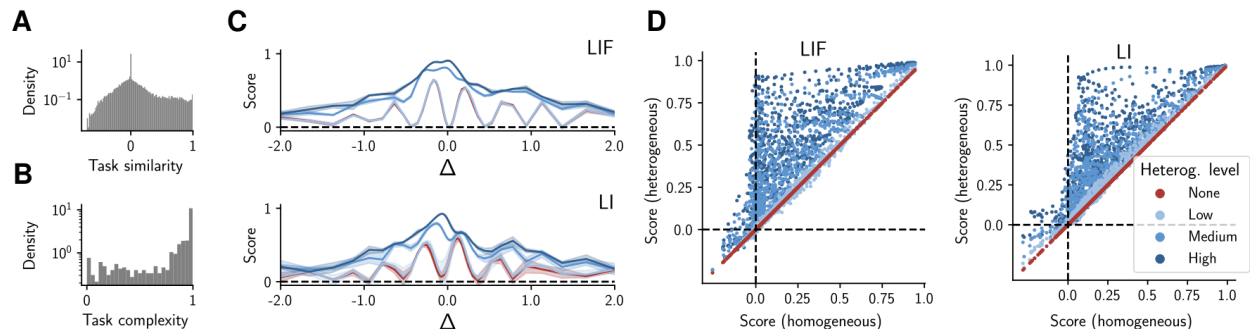


Figure 2: Intrinsically heterogeneous networks process chaotic time series more accurately. The task family $y_\theta = u_k(t + \Delta)^d$ was used to generate 882 tasks with parameters drawn from the ranges $d \in \{1, \dots, 6\}$, $\Delta \in [-2, 2]$, and $k \in \{1, 2, 3\}$. Performance of all networks was evaluated on each of these tasks. (A) Distribution of cosine *similarities* between all task pairs; most pairs are orthogonal and therefore temporally independent. (B) Task complexity is defined as the cosine *dissimilarity* between the target function $u_k(t + \Delta)^d$ and its source input $u_k(t)$. This definition assigns a minimal complexity of 0 to the identity (or pure-relay) task, which requires neither memory ($\Delta = 0$) nor nonlinear processing ($d = 1$). Tasks in \mathcal{F}_θ therefore span a broad spectrum of complexities. (C) Performance profiles for a subset of parameters corresponding to quadratic ($d = 2$) recall ($\Delta < 0$) and forecasting ($\Delta > 0$) of the first ($k = 1$) input component. The top and bottom panels show the results for spiking (LIF) and rate-based (LI) implementations, respectively. Shaded area show 10-fold enlarged standard deviation estimated over three independent trials. (D) Direct score comparison between homogeneous (x-axis) and heterogeneous (y-axis) networks for each task (each dot). Colors indicate the degree of heterogeneity. The diagonal dotted line marks equal performance, while the vertical and horizontal dashed lines denote the chance-level score. The right-hand panel corresponds to the spiking implementation and the left-hand panel to the rate-based implementation. Panels (C) and (D) share the same color code.

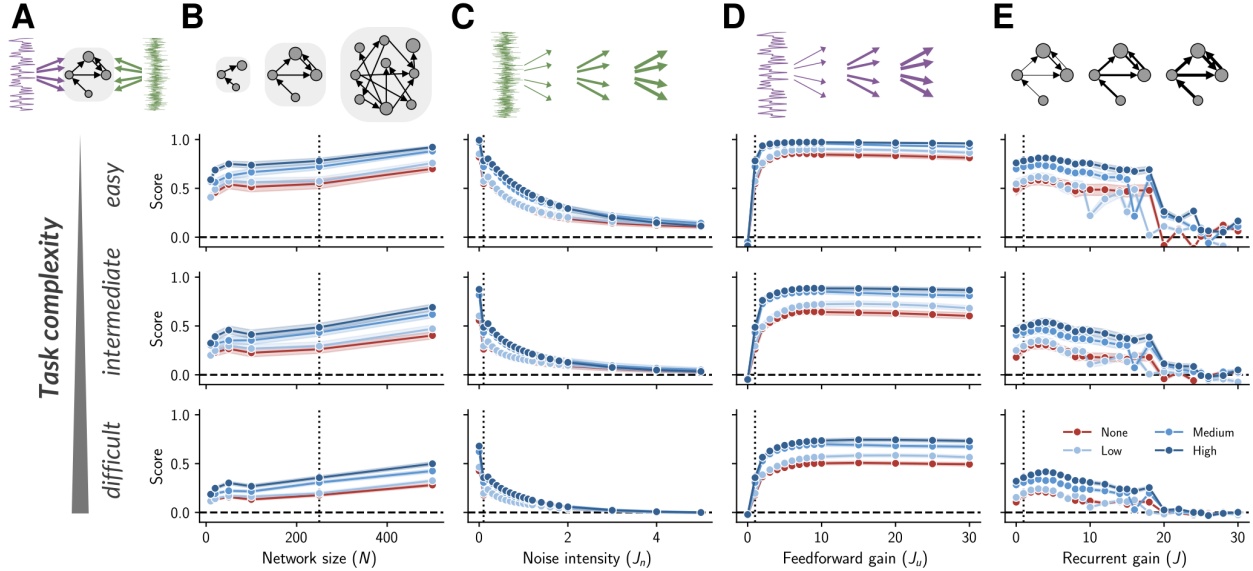


Figure 3: Neuronal heterogeneity renders networks robust. (A) (Top) Schematic of the network and its inputs. Purple and green traces represent the deterministic input and stochastic noise that are projected onto the network at its center. (Bottom) Tasks are divided into three complexity tiers (indicated by the gradient), and performance is averaged within each tier for clarity. (B–E) (Top) Schematic of the varied hyperparameters; see panel (A) for reference. (Bottom) Impact of varying network size (B), noise intensity (C), feedforward gain (D), and recurrent gain (E) on the performance of rate-based RNNs. All panels use the same color code. The plateaus in panel (D) arise from saturation of neuronal activity. The uniform decline of the score at large recurrent-gain values in panel (E) reflects a transition to chaos. Analogous results for spiking networks are shown in Fig. S.7. In all panels dots represents the simulated hyperparameters and the shaded area indicate 95% confidence interval, calculated over tasks belonging to the corresponding complexity tier.

We first examined how network size N influences the performance profile. Because reservoir computers are universal approximators [53–55], larger networks generally achieve higher performance. In the limit $N \rightarrow \infty$, the random recurrent coupling among neurons is guaranteed to generate an arbitrarily rich dynamical landscape, sufficient to approximate any function regardless of the network’s heterogeneity level. Real networks, however, are finite ($N < \infty$) and therefore perform less optimally. Consequently, a key question is whether heterogeneity can rescue the performance of such finite networks that do not satisfy the assumptions of the universality theorem. As Fig. 3B (and Fig. S.7B) shows, the average performance of heterogeneous rate-based (respectively spiking) networks is superior to that of their homogeneous counterparts across all sizes and complexity tiers. Complexity tiers are defined by dividing the full complexity value range (0-1) into three equal-width intervals. Task with complexity values in the lower, middle, and upper thirds are labeled respectively as easy, medium, and hard. Remarkably, networks as small as $N = 50$ neurons, when highly heterogeneous, outperform a homogeneous network ten times larger in every task tier. This indicates that time-constant heterogeneity is an effective strategy for recreating a rich dynamical repertoire and rescuing performance in the small-size regime.

Next, we asked whether heterogeneous networks, like biological organisms, are robust to strong stochastic stimuli. To answer this question we varied the noise intensity J_n (the standard deviation of the fluctuations) from 0 (no noise) to 5 (corresponding to a signal-to-noise ratio of 0.2) and repeated the experiments. As shown in Fig. 3C (and Fig. S.7C), heterogeneous rate-based and spiking networks outperform their homogeneous counterparts at all noise levels. Thus, although they are not immune to extreme noise, they exhibit markedly greater resilience.

We then examined the effects of the feed-forward gain J_u (from the input to the network) and the recurrent gain J (within the network), which together determine the dynamical regime of the RNN. When $J_u \gg J$, the network is effectively input-driven. Moreover, if J is sufficiently small, the network exhibits a fading-memory condition: whether or not input is present, any memory of the initial state gradually fades away. In this input-driven regime, the fading-memory condition [53, 56] (also known as the echo-state property [57], contractive dynamics [58], or dissipative dynamics [59]) is particularly desirable for working-memory-like input-output associations (as defined in Section 2.2), because such mappings can be learned without interference from the internal state.

Conversely, when $J_u \ll J$, the network operates in a largely state-driven (autonomous) regime, in which the next state of the network is dictated primarily by its previous state rather than by the external input. At the extreme,

very strong recurrence gives rise to chaotic activity [60], which is undesirable for systems that must implement working-memory-like input-output associations with dynamic states. In practice, a moderate level of recurrence is necessary to ensure the richness of the dynamical repertoire, supporting memory maintenance, and nonlinear processing required by the task.

As Fig. 3D shows for the rate-based networks (and Fig. S.7D for the spiking RNNs), increasing the feed-forward gain J_u improves performance across all complexity tiers. A larger J_u pushes the network toward an input-driven regime, making the input-output association easier. Nevertheless, even at very high J_u values, the maximal performance of homogeneous networks remains lower than that of highly heterogeneous networks for almost all J_u levels.

Fig. 3E and Fig. S.7E summarize the effect of varying the recurrent gain J in the rate-based and spiking RNNs, respectively. As before, heterogeneous networks uniformly outperform their homogeneous analogs in both implementations. Moreover, as expected, very strong recurrence prevents any meaningful association between input and output. For the rate-based networks, the abrupt performance drop at $J_c \approx 18$ marks the critical recurrence value at which all networks—regardless of heterogeneity level—transition into an autonomous chaotic state. This critical value, however, is considerably higher for spiking RNNs (cf. Fig. S.20G). Yet, apart from the uniform superiority of heterogeneous networks and the abrupt performance drop associated with the transition to chaos, Fig. 3E and Fig. S.7E reveal another striking pattern. As discussed earlier, for tasks requiring memory and non-linear processing, a non-zero J is necessary. Consistent with this view, for the collection of tasks defined by our benchmark, the average performance of the rate-based networks peaks at an intermediate value $J < J_c$. However, even at this optimal J , homogeneous networks still lag far behind heterogeneous systems that have no recurrent communication at all ($J = 0$). This suggests that enriching the dynamical repertoire by tuning the recurrent gain J is far less effective than the enrichment provided by heterogeneous neurons.

Further, we investigated how the structure of the recurrent connectivity influences performance, by varying the network’s sparsity p , the excitatory-to-inhibitory population ratio f , and the recurrent-weight dispersion σ_0 . For a fair comparison, each of these factors is swept while preserving the overall excitatory-to-inhibitory balance of the network. Note that this balance between inhibitory and excitatory populations is controlled by the mean of the population-specific weights and is independent of their variance (dispersion). The variance, however, determines how strictly Dale’s law is obeyed. Low weight dispersion means that synapses originating from a given population have similar polarity (all inhibitory or all excitatory), as in the classical formulation of Dale’s law [61]. In contrast, high weight dispersion allows a population to project synapses of mixed polarity, even though the average weight conforms to the population’s identity—effectively implementing a “soft” Dale’s law. Figures S.8B–D and S.9B–D summarize the effects of changing these recurrent-related hyperparameters. Interestingly, neither sparsity nor weight dispersion affect performance and heterogeneous networks outperform their homogeneous version.

Note that in general network performance depends on the sampled data, resulting in a level of uncertainty in the measured performance. To capture this uncertainty, we trained three independent readouts for each network using non-overlapping time intervals (trials), evaluated their performance on the same test set, and used the variance of the performance scores as a proxy for uncertainty. We repeated this procedure for all network configurations and tasks, and we summarize the results in Fig. S.17 and Fig. S.18 for the rate-based and spiking systems, respectively. In both figures, heterogeneous networks exhibit performance variance that is comparable to or lower than that of homogeneous networks; however, in all cases the uncertainty is significantly lower than the measured performance.

2.5 Heterogeneity saves energy on various computing systems

In the previous section we showed that heterogeneity enables even small, weakly coupled networks to perform well. Consequently, using such simple heterogeneous networks—in place of large, densely coupled homogeneous ones—can reduce energetic cost without compromising performance. Energy minimization is a key objective for artificial, biological, and emerging neuromorphic systems. Therefore, we defined and estimated hardware-dependent energy costs for our rate- and spiking-based implementations, as well as for two neuromorphic chips (Loihi 2 and SpiNNaker 2). The energy calculations and the neuromorphic implementations are described in Sections A and 4.8, respectively.

To quantify the cost savings induced by heterogeneity, we identified, at each performance level, the minimum cost E^* among a pool of networks with varying sizes. As Fig. 4 shows, the remarkable performance of small heterogeneous networks enables them to achieve high scores at only a fraction of the cost incurred by homogeneous networks—a result that holds across all computing platforms. Although higher performance levels typically require greater energy consumption (see also [62, 63] for biological evidence), heterogeneity mitigates this increase by orders of magnitude.

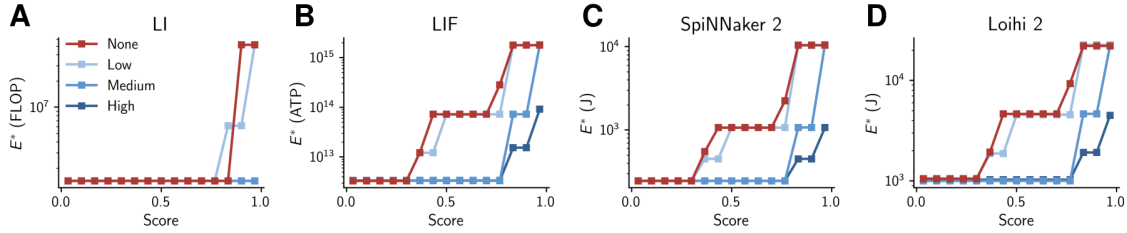


Figure 4: Heterogeneity lowers the cost at each performance level. At every performance bin, the network with minimal energy consumption (E^*) is the most efficient. In all systems, heterogeneity substantially reduces the total minimal cost (note the logarithmic scale of the y-axis). This cost saving primarily results from using equally performant networks that are much smaller. The definition of cost for each hardware system reflects its specific characteristics. We used (A) the total number of floating-point operations (FLOPs) and the memory footprint for rate-based networks, and (B) the total expenditure of adenosine triphosphate (ATP) molecules in biological spiking networks. For neuromorphic systems, (C) Loihi 2 and (D) SpiNNaker 2, the total energy consumption (in joules) was estimated based on direct measurements of their power usage.

2.6 Heterogeneity can act as an inductive bias

In our simulations, heterogeneity is quantified by the dispersion of neuronal membrane time constants. However, we imposed this heterogeneity in a very specific way: we fixed the mean time constant at the nominal value $\mathbb{E}[\tau] = 1$ and drew individual time constants from a log-normal distribution. Because heterogeneity has a substantial impact on performance, a question is how altering the heterogeneity profile itself affects performance. To address this, we relaxed both constraints. First, we systematically shifted the mean $\mathbb{E}[\tau]$ to smaller or larger values (corresponding to faster or slower stimulus-integration rates, respectively). Second, we sampled time constants from alternative distributions whose parameters were chosen so that their empirical mean and variance match those of the original log-normal distribution. Figure 5 summarizes the results for networks with various degrees of heterogeneity in both the rate-based and spiking implementations.

Fig. 5A shows that both spike- and rate-based RNNs achieve higher overall accuracy when the mean time constant satisfies $\mathbb{E}[\tau] < 1$. Importantly, if $\mathbb{E}[\tau]$ is chosen appropriately, even homogeneous RNNs can perform well. Although one could search for the optimal $\mathbb{E}[\tau]$ for a fixed, known collection of tasks in a post-hoc manner, such a brute-force search is rarely desirable (because of its high computational cost) and often infeasible (tasks are numerous, may be novel, and can have distinct computational demands that require non-overlapping time-constant distributions). It is precisely in this context that task-agnostic parameter heterogeneity proves beneficial. By diversifying neuronal resources across a wide range of values, the network remains functional on diverse tasks without any task-specific optimization. Thus, intrinsic heterogeneity acts as an inductive bias that enhances the generalization capability of the network across various tasks.

Nevertheless, as illustrated in Fig. 5B, not all heterogeneity distributions are equal. Similar experiments using gamma, normal, and uniform distributions show that skewed distributions result in highest performance. This suggests that performance increases by heterogeneity is feasible when the underlying distribution permits a broad, skewed, non-localized range of time-constant values.

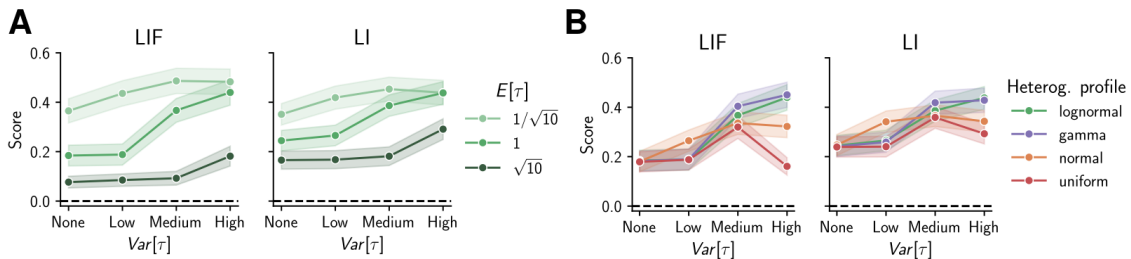


Figure 5: The heterogeneity profile substantially affects generalization. (A) At any given value of $\mathbb{E}[\tau]$, heterogeneity improves performance. By spreading neuronal time constants over a broader interval, heterogeneity increases the likelihood of covering the regions required by the tasks. (B) The performance depends on the heterogeneity profile. Skewed distributions (log-normal and gamma) result in higher performance levels. The empirical mean and variance were identical for all profiles. The shaded area in (A) and (B) correspond to indicate 95% confidence interval across all tasks.

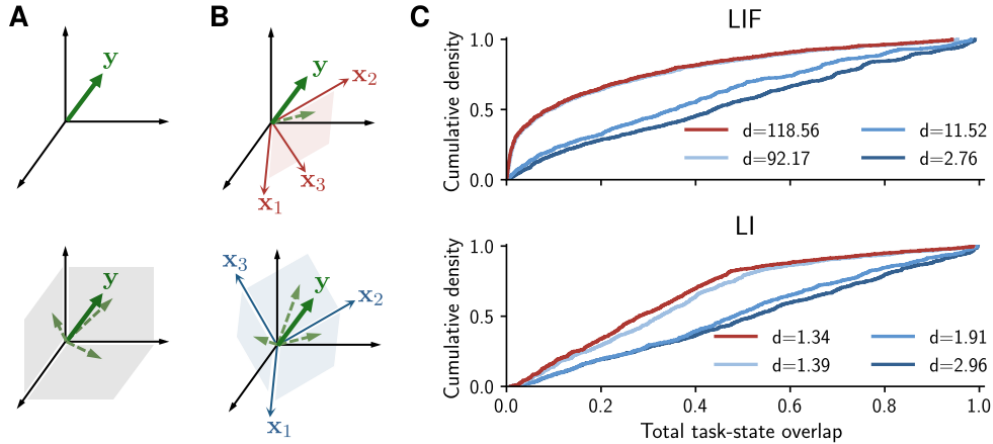


Figure 6: Heterogeneity increases temporal alignment between tasks and the network’s state (A) (top) Any temporal task $y(t)$ can be regarded as a high-dimensional vector y in an appropriate vector space. (bottom) Decomposition of the task vector y into its independent components; in this example three components are sufficient to represent y . (B) Network states form a basis that spans a subspace of this vector space. (Top) State of an exemplar network that spans only a two-dimensional subspace, thereby capturing only the task’s projection onto that subspace (the dashed arrow). (Bottom) Basis set generated by another network that spans a three-dimensional subspace, fully embedding y and thus reconstructing the task completely. (C) Direct assessment of temporal alignment between network states and all tasks. An alignment score of 0 indicates that the subspace spanned by the state is orthogonal to a task, whereas a score of 1 means the task lies entirely within that subspace. The curves show the cumulative distribution of this alignment score across tasks. The dimensionality of each network state, estimated by the participation ratio, is indicated in the legend. Note that higher performance does not necessarily correspond to the highest dimensionality. Neural states are decorrelated before computing alignment.

2.7 Heterogeneity improves the task-state alignment

While the network’s nonlinearities prevent us from analytically predicting the impact of diverse time constants, it is nevertheless straightforward to quantify this effect empirically. Since linear readouts of the network state $X(t)$ are used to reconstruct the target function $y(t)$, performance will be high when the (independent) modes of $X(t)$ align temporally with those required by $y(t)$. In other words, performance is high if the vector y (obtained by concatenating all time points) lies in the column space of $X(t)$ (see Fig. 6A–B).

We measured the alignment for all network–task pairs and plotted the network-specific alignment distribution (aggregated over all tasks) in Fig. 6C. The systematic shift of the distributions toward higher values indicates that larger heterogeneity is associated with stronger task-state alignment.

It is also worth noting that, although task–state alignment directly gauges performance by quantifying the temporal correspondence between the two (see Section C for discussion), the dimensionality of the state does not always correlate with performance. By computing the effective dimensionality of the state using the participation ratio, we observe that the higher performance achieved by heterogeneous networks is accompanied by a dimensionality expansion in rate-based networks, but by a reduction of dimensionality in spiking RNNs. In summary, neuronal heterogeneity affects both the state’s dimensionality and its alignment with the task. However, only the latter—state-task alignment—causally determines performance.

3 Discussion

Neuronal heterogeneity is a ubiquitous property of biological systems [2–4, 6–11] that plays a crucial role in shaping neuronal firing patterns [12, 16], modulating coding efficiency [13, 17, 21], fine-tuning motor-gain control [14, 15, 19], and enhancing responsiveness [23, 24]. Thus, understanding how neuronal heterogeneity operates within neural networks is of great computational importance.

A number of recent machine-learning studies have demonstrated that a task-guided, top-down optimization of neuronal heterogeneity yields performance equal to or better than that of homogeneous networks trained on the same tasks [31–35, 64]. This task-induced organization, however, appears biologically implausible [36, 37, 65] and is computationally very demanding [33]. Although the biological implausibility can be circumvented at the synaptic level [66–70], at the neuronal level credit assignment would require activity-dependent modulation of passive biophysical

or morphological features, which is at odds with their stability throughout adulthood [40, 41]. An alternative to this task-guided organization is a bottom-up, task-agnostic parameter distribution. While this resolves the implausibility issues, it is not immediately clear whether a system with such task-agnostic heterogeneity can perform any useful computation. We addressed this question by investigating how the level of intrinsic heterogeneity affects the performance of recurrent neural networks across hundreds of working-memory-like tasks. Importantly, in contrast to classical deep-learning paradigms—where task-specific end-to-end training reshapes the network’s internal dynamics—we adopted the reservoir-computing paradigm [53, 57], which leaves the internal dynamics unchanged by training.

By coupling chaotic stimuli with a parameterized nonlinear mapping, we curated a comprehensive benchmark that is low-bias and has high discriminative power, consisting of hundreds of dissimilar tasks spanning a wide range of complexities (Figs. 2A–B, S.4A–B, S.5A–B, and S.6A–B). This benchmark allows us to assess the role of neuronal heterogeneity in a task-independent manner, addressing a key limitation of previous studies [31–35, 64] that examined only a handful of tasks. Our findings reveal that, in both rate- and spike-coded networks, heterogeneous RNNs—despite possessing a task-agnostic parameter organization—significantly outperform their homogeneous counterparts (cf. Fig. 2, S.4, S.5, and S.6), exhibit lower performance variability (Fig. S.17 and S.18), and are more robust to a variety of internal and external perturbations (Fig. 3, S.7, S.8, and S.9). Consequently, our work extends earlier observations on the benefits of neuronal heterogeneity [25, 33] to a much broader domain.

Further we demonstrate the energetic advantage of heterogeneity in both biological and artificial systems. We show that small yet heterogeneous networks outperform much larger homogeneous RNNs (Fig. 3B and S.7B), thereby saving substantial cost without sacrificing performance (Fig. 4). Importantly, this energetic benefit is implementation-independent and has profound implications for neuroscience, machine learning, and neuromorphic computing, which we discuss briefly below.

From the neuroscientific perspective, this work offers an explanation for the evolutionary function of task-agnostic intrinsic heterogeneity. By enhancing robustness and lowering metabolic cost, intrinsic heterogeneity enables even simple organisms—with simple nervous systems—to carry out a plethora of vital computations, thereby increasing their fitness. Because this advantage persists across all brain sizes, many species could have exploited and preserved it throughout evolution, which also explains the ubiquity of heterogeneity across the animal kingdom.

The machine-learning community benefits from our work in two ways: (1) heterogeneous parameter initialization and (2) the introduction of diversity among artificial units. As alluded to in earlier studies [33] for a single task, heterogeneous parameters—even when omitted from training—reduce training cost. This stems from the inherently higher dynamical expressivity of heterogeneous systems (see below). Our results confirm that this benefit is not task-dependent; other temporal tasks can also enjoy lower training costs. Moreover, a far more intriguing avenue is to embed heterogeneity directly in the properties of artificial units [71] (e.g., through diverse activation functions [72] or varied architectures and routing [73]) as inductive biases [50] that enhance the expressivity of untrained models.

The energetic aspect of our findings is particularly relevant for neuromorphic applications, where low resource usage and simple architectures are primary constraints. Exploiting—rather than suppressing—the large device-to-device variability that is common in analog devices [74–76] can potentially improve performance, robustness, and energy efficiency while simultaneously reducing fabrication and quality-assessment costs.

The benefit of intrinsic heterogeneity stems from enriching the dynamical repertoire of neural activity, thereby increasing its expressivity. Classically, recurrent connections are added to networks to enable memory maintenance. The same computational need can also be satisfied by heterogeneous neurons that integrate the stimulus at different rates, each preserving a distinct memory trace of the same input. An illustrative example is shown in Fig. 3E, where fully decoupled heterogeneous systems outperform recurrently connected networks with homogeneous units. This highlights the capacity of neurons—rather than synaptic connections—to generate rich dynamics by forming a filter bank, a principle long known to engineers (e.g., [77], Ch. 7) but underappreciated by connectionists.

Intrinsic diversification is a natural strategy when the computational demands—and thus the optimal parameters—are unknown, or when the network must perform multiple (possibly novel) computations (cf. Fig. 5A). By distributing neuronal resources across a wide range of time constants, heterogeneity eliminates the need for further parameter optimization, thereby addressing both the high optimization cost [33] and the catastrophic-forgetting problem [38, 39].

It is, however, important to note that not all heterogeneity profiles are equivalent (c.f. Fig. 5B). A profile that restricts time constants to a narrow range (e.g., normal or uniform distributions) may fail to cover the requirements of all tasks, leading even a highly heterogeneous network to perform suboptimally. This explains why studies that impose localized heterogeneity (e.g., [78]) report inconclusive effects. In contrast, highly skewed profiles that produce parameters spanning several orders of magnitude are more likely to satisfy the demands of a diverse task set. Notably, [33] observed that the distributions of neuronal time constants in mice and humans are strongly skewed [4, 9, 79], consistent

with this argument. Nevertheless, the precise relationship between different skewed profiles and task demands remains an open question for future investigation.

While we focused here on heterogeneity of the membrane time constant, diversity in other temporal parameters—such as synaptic delays, synaptic response kinetics, postsynaptic-receptor turnover, vesicle-recycling rates, and so on—may produce similar effects. For example, Sun et al. [80] demonstrated successful execution of temporal tasks by optimizing axonal delays, Winston et al. [34] investigated the same problem by tuning the after-spike current, and Habashy et al. [64] showed that both delays and neuronal time constants can be equivalently tuned to achieve optimal performance. Given the well-documented hierarchy of timescales in the brain [81, 82], it is likely that this diversification principle is employed across different brain regions to support a variety of cognitive tasks. Indeed, other perceptual modalities also benefit from heterogeneity. A classic example is the mammalian visual cortex, where heterogeneity in orientation selectivity in V1 enables animals to detect all possible orientations [83, 84]. Similar principles have been proposed for the olfactory system [85, 86], auditory system [87–90], and somatosensory system [91, 92], as well as for spatial encoding via grid cells [93]. The role of cellular and subcellular heterogeneity is not limited to high-level cognitive functions. For instance, recent work [94] showed that perturbing the regulators of cell-type diversity in the mouse cerebellar cortex prevents hemisphere formation during development. These observations, together with the robustness benefits reported here, suggest that intrinsic heterogeneity serves as a biological inductive bias [50, 95]—rather than an undesirable imperfection—enabling organisms to generalize across a wide variety of tasks and novel conditions.

In conclusion, this work elucidates the functional role of neuronal heterogeneity at the network level, with substantial implications for neuroscience, machine learning, and neuromorphic computing. The pronounced advantage conferred by intrinsic heterogeneity underscores the importance of incorporating beyond-mean, second-order effects when studying the mind and when designing brain-inspired devices and algorithms.

4 Methods

4.1 Networks configuration

Each network consists of N neurons, each belonging to either an excitatory (E) or inhibitory (I) subpopulation. A fraction f of the neurons are excitatory. Neurons are connected randomly and sparsely with connection probability p . We do not fix the in- or out-degree of any neuron; consequently, the number of synapses fluctuates around the expected value Np . Autapses are prohibited. The K -dimensional feedforward input is projected onto the network via fixed, dense, random connections w_{ik}^u , whose values are drawn from a standard normal distribution.

Within the network, the synaptic weight from neuron j to neuron i is denoted by w_{ij} and remains constant. Its value is drawn from a population-specific Gaussian distribution with mean μ_x and variance σ_x^2 ($x \in \{E, I\}$); the sign of the weight determines its polarity (excitatory or inhibitory). The means of these Gaussian distributions are chosen so that the network is in balance [96, 97], i.e.:

$$f\mu_E + (1 - f)\mu_I = 0. \quad (1)$$

Note that, unlike [98], our networks are in a loose balance, which aligns better with measurements in the cerebral cortex [99] (see also [100]). For simplicity, the synaptic-weight variance σ_x^2 is kept the same for both populations:

$$\sigma_I^2 = \sigma_E^2 = \sigma_0^2. \quad (2)$$

We refer to this as weight dispersion. As in [97, 101], to ensure that input fluctuations are independent of network size, recurrent weights are scaled by J/\sqrt{Np} , where J is a global recurrent gain that modulates the strength of internal connections. Similarly, feedforward weights are scaled by J_u/\sqrt{K} , which makes the variance of the external input independent of its dimensionality while allowing the overall input strength to be adjusted via J_u . Finally, each neuron receives independent and identically distributed (i.i.d.) white noise, whose intensity is controlled by J_n .

4.2 Stimulus synthesis

For the majority of our simulations, we used the solution of the Lorenz system [51], described by

$$\dot{x} = \sigma(y - x), \quad (3)$$

$$\dot{y} = x(\rho - z) - y, \quad (4)$$

$$\dot{z} = xy - \beta z. \quad (5)$$

The Lorenz system is a well-known chaotic system; with parameters $\rho = 28$, $\sigma = 10$, and $\beta = 8/3$, its trajectory lies on a chaotic attractor. To minimize transient behavior, we chose the initial conditions $(x_0, y_0, z_0) = (-1.96582031, -1.08886719, 2.17578125)$, a point close to the stable manifold.

A second stimulus was generated by concatenating three one-dimensional time series obtained from Mackey–Glass system [102], a delayed differential equation given by:

$$\dot{x} = \frac{ax(t - \delta)}{1 + x(t - \delta)^n} - bx(t). \quad (6)$$

For the commonly used parameter values $a = 0.2$ and $b = 0.1$, delay parameters $\delta \lesssim 16.5$ produce periodic orbits, whereas $\delta \gtrsim 17$ generate chaotic trajectories [103]. The full stimulus was constructed using three delay values, $\delta = 10, 50, \text{ and } 80$. In all cases we set the initial condition $x_0 = 1.2$ and sampled a random history uniformly from $[1.1, 1.3]$ for the preceding time steps up to $-\delta$.

The trajectories of both the Lorenz and Mackey–Glass systems were generated by numerically integrating their respective equations using the Runge–Kutta 4/5 (RK45) method.

We also employed two additional stimuli with high and very low predictability, respectively: a periodic input $u(t) = |\sin t|$ and the nonlinear autoregressive moving-average (NARMA) model [104]. The NARMA system is a discrete-time dynamical system described by

$$u[t + 1] = a_1 u[t] + a_2 \sum_{i=0}^{n-1} u[t] u[t - i] + b \xi[t - (n - 1)] \xi[t] + c \quad (7)$$

with ξ being a uniform random variable in $[0, 0.5]$ and n indicating the order of the model. We used parameters $a_1 = 0.2$, $a_2 = 0.04$, $b = 1.5$, $c = 0.001$, zero initial conditions, and a model order of $n = 30$. This discrete signal is then interpreted as samples of a continuous stimulus with time step Δt , i.e., $u[i] = u(i\Delta t)$. For all stimuli, values at arbitrary times were obtained by linear interpolation.

The choice of parameters in the dynamical systems above affects the amplitude and temporal characteristics of the resulting trajectories. Thus, for a fair comparison each component was first standardized and then temporally rescaled so that the overall timescale of the compound stimulus equals 1, i.e., the average membrane time constant of our networks. Concretely, we computed the power spectrum of each component independently, identified the frequency with maximal power, and defined a compound frequency as the geometric mean of these peak frequencies. Time was then uniformly scaled for all components such that the compound frequency becomes 1 Hz. With this scaling we ensure that the network and the input, on average, operate on similar time scales, although either system can still exhibit much shorter or much longer temporal dependencies.

4.3 Neuronal dynamics

We implemented two neuronal dynamics: the rate-based leaky integrator (LI) and the spiking leaky integrate-and-fire (LIF) models.

For the LI dynamics, the membrane voltage of the i -th neuron, v_i , evolves according to

$$\tau_i \frac{dv_i(t)}{dt} = -v_i(t) + \frac{J}{\sqrt{Np}} \sum_{j=1}^N w_{ij} r(v_j(t)) + \frac{J_u}{\sqrt{K}} \sum_{k=1}^K w_{ik}^u u_k(t) + J_n \xi_i(t), \quad (8)$$

$$r(x) = [1 + \exp(-x)]^{-1}. \quad (9)$$

Here τ_i is the neuron-specific membrane time constant, $r(\cdot)$ is a static sigmoidal nonlinearity (activation function), $u_k(t)$ is the k -th component of the external stimulus, and $\xi_i(t) \sim \mathcal{N}(0, 1)$ is neuron-specific white noise. Throughout this work we use a strictly positive sigmoidal activation function, although other nonlinearities are possible. The function $r(\cdot)$ is interpreted as the (max-)normalized firing rate (hence unitless), whereas the recurrent and feedforward weights w_{ij} and w_{ik}^u have the same units as the membrane potential v_i . Importantly, the gains J and J_n scale the recurrent input and noise amplitude, respectively.

For the LIF model the membrane voltage of the i -th neuron evolves according to

$$C_i \frac{dv_i(t)}{dt} = g_L(E - v_i(t)) + I_{bg} + \frac{g_{rec}}{\sqrt{Np}} \sum_{j=1}^N w_{ij} s_j(t) + \frac{g_{ff}}{\sqrt{K}} \sum_{k=1}^K w_{ik}^u u_k(t) + g_L J_n^2 \xi_i(t)$$

C_i denotes the neuron-specific membrane capacitance, while the reversal potential E , the leak conductance g_L , and the recurrent (g_{rec}) and feedforward (g_{ff}) conductances are assumed to be identical across neurons. A constant background current I_{bg} is introduced to make the LIF dynamics comparable to the LI dynamics (see below). The term $s_j(t)$ represents the post-synaptic potential triggered by presynaptic spikes. A LIF neuron emits a spike when its membrane voltage reaches the threshold v_{thr} , after which the voltage is reset to v_{reset} . To cap the maximal possible activity—analogueous to the saturating activation function in the rate model—the membrane potential is held at v_{reset} for an absolute refractory period τ_{ref} . These dynamics can be summarized by the following set of equations:

$$\tau_i \frac{dv_i(t)}{dt} = -v_i(t) + (v_{\text{bg}} - E) + \frac{J}{\sqrt{Np}} \sum_{j=1}^N w_{ij} s_j(t) + \frac{J_u}{\sqrt{K}} \sum_{k=1}^K w_{ik}^u u_k(t) + J_n \xi_i(t), \quad (10)$$

$$s_j(t) = \tau_{\text{ref}} \sum_f \delta(t - t_j^f), \quad (11)$$

$$t_j^f = \arg v_j(t) = v_{\text{thr}}, \quad (12)$$

$$v_j(t) = v_{\text{reset}}, \quad t \in (t_j^f, t_j^f + \tau_{\text{ref}}], \quad (13)$$

where the neuron-specific membrane time constant is $\tau_i = C_i/g_L$, and the global recurrent and feedforward gains, $J = g_{\text{rec}}/g_L$ and $J_u = g_{\text{ff}}/g_L$, correspond to their rate-based analogs. For computational efficiency we model synapses as instantaneous elements (Eq. 11); however, temporally extended synaptic kernels (e.g., $s_j(t) = \kappa(t) * \sum_f \delta(t - t_j^f)$ with standard kernel functions) are equally valid. The factor τ_{ref} in Eq. 11 ensures that the voltage increment produced by a single spike during the refractory period τ_{ref} matches the increment generated by the rate model with a saturating activation function over the time interval.

The dynamics of LI and LIF neurons can be matched using several strategies, each requiring coordinated tuning of different parameters. Here we focus on aligning the dynamical range of the two neuron models, as described shortly. For alternative approaches, see Section B.

The voltage of a LIF neuron is bounded above by the threshold v_{thr} (i.e., $v_i \leq v_{\text{thr}}$), whereas the voltage of an LI neuron is unbounded. In both cases, however, only a limited voltage interval carries the relevant coding information. For a LIF neuron this interval is $[v_{\text{reset}}, v_{\text{thr}}]$, and for an LI neuron with the sigmoidal activation function of Eq. 9 it is $[-0.5, 0.5]$. Any pair of values that differ by one unit (e.g., a 1-mV difference) between v_{reset} and v_{thr} satisfies this condition. We arbitrarily chose $v_{\text{reset}} = E = -70$ mV and $v_{\text{thr}} = -69$ mV and set the absolute refractory period to $\tau_{\text{ref}} = 2$ ms. The background input v_{bg} is tuned so that, at rest, the LIF neuron fires at a baseline rate $\nu_0 = 5$ Hz. This input is neuron-specific and can be computed directly from Eq. 14.

$$v_{\text{bg},i}(\nu) = \frac{(v_{\text{reset}} - E)z_i - (v_{\text{thr}} - E)}{z_i - 1}, \quad (14)$$

$$z_i = \exp\left(\frac{1}{\nu\tau_i} - \frac{\tau_{\text{ref}}}{\tau_i}\right) \quad (15)$$

which is found by solving the generic form of $\nu - I$ relation (presented in Eq. S.9) for the background current.

4.4 Integration details

All networks were initialized at zero and integrated with the explicit Euler method using a time step of $\Delta t = \frac{\mathbb{E}[\tau]}{100} = 0.01$. This step size balances numerical accuracy (it is sufficiently small relative to the neuronal time constants) with computational efficiency (it is large enough to make long simulations feasible). Only for a few networks did this step size produce inaccurate integration, which was diagnosed by an anomalous performance profile across all tasks. In those cases the system was reintegrated with a Runge–Kutta integrator, and the dense solution was sampled at intervals of Δt to maintain the same sampling rate across all networks.

All networks are integrated for $L = L_{\text{train}} + L_{\text{test}}$ time steps, and the results are saved to disk for later training and evaluation. For LIF networks, we saved the spike trains. For LI networks, the neuronal voltages were stored with 16-bit floating-point precision to reduce the storage load (compared with the 64-bit precision used during the simulations). Although some information is lost during this conversion, we anticipate that its effect on performance will be minimal, as demonstrated in artificial systems [105, 106] and computational studies [107].

4.5 Datasets, optimization, and performance quantification

The lengths of the training (L_{train}) and test (L_{test}) subsets must be sufficiently long to provide enough samples for reliable read-out optimization and an unbiased assessment of within-distribution generalization. Assuming that the

tasks evolve on an average timescale τ_y , we require the training and test intervals to span at 20 and 10 *oscillations* of that timescale, respectively. Moreover, because larger networks contain more learnable parameters, we scale the training duration proportionally to the number of neurons. With these criteria, the numbers of time steps in the training and test subsets are, respectively,

$$N_{\text{train}} = (N + 1) \frac{20\tau_y}{\Delta t}, \quad (16)$$

$$N_{\text{test}} = \frac{10\tau_y}{\Delta t}. \quad (17)$$

However, because of the structure of our tasks, the training and test subsets must be longer. We evaluate the networks on memory-recall and forecasting tasks up to a maximal temporal horizon of $2\tau_u$. Consequently, for every time point in the training and test sets, the target function must be available $2\tau_u/\Delta t$ steps both in the past and in the future. Hence, the total lengths of the subsets are

$$L_{\text{train}} = N_{\text{train}} + \frac{4\tau_u}{\Delta t} = (N + 1) \frac{20\tau_y}{\Delta t} + \frac{4\tau_u}{\Delta t}, \quad (18)$$

$$L_{\text{test}} = N_{\text{test}} + \frac{4\tau_u}{\Delta t} = \frac{10\tau_y}{\Delta t} + \frac{4\tau_u}{\Delta t}. \quad (19)$$

Since all tasks are generated from a stimulus whose overall timescale is $\tau_u = 1$ (see Section 4.2), we assume that the temporal variation of the target inherits this same timescale. Consequently, we set $\tau_y = 1$.

The training and test datasets are constructed by pairing the network states with the corresponding target functions. For rate-based networks, the state $\mathbf{X}(t)$ is obtained by passing each neuron’s membrane voltage through the activation function (9). For spiking networks, the spike trains are first convolved with an exponential kernel (see Eq. 11)

$$\phi(t) = \exp(-t/\tau_\phi), \quad \tau_\phi = 10\Delta t,$$

to produce a continuous-time representation of the state. We varied the kernel’s time constant (over $\tau_\phi \in [5, 100] \Delta t$) and kernel shapes (alpha and Gaussian). In none of these cases did we observe any qualitative difference in performance profiles.

All 882 time-aligned target functions are stacked into the matrix $\mathbf{Y}(t)$, yielding a dataset $\mathcal{D} = \{\mathbf{X}(t), \mathbf{Y}(t)\}$ for each network. The dataset is then split into training and testing subsets of lengths L_{train} and L_{test} , respectively. From each subset we extract the central N_{train} and N_{test} samples and temporally shuffle them to remove transient effects, producing the state–target pairs $\mathcal{D}_{\text{train}} = \{\mathbf{X}_{\text{train}}, \mathbf{Y}_{\text{train}}\}$ and $\mathcal{D}_{\text{test}} = \{\mathbf{X}_{\text{test}}, \mathbf{Y}_{\text{test}}\}$.

The optimal linear read-out $\beta_\theta \in \mathbb{R}^{N+1}$ for the state matrix $\mathbf{X}_{\text{train}} \in \mathbb{R}^{(N+1) \times N_{\text{train}}}$ (including the bias) that approximates a task with parameters θ (i.e., $\mathbf{y}_{\theta, \text{train}} \in \mathbb{R}^{N_{\text{train}}}$) is obtained by minimizing the objective function

$$\mathcal{L}_\theta(\beta) = \|\mathbf{y}_{\theta, \text{train}} - \beta^T \mathbf{X}_{\text{train}}\|^2 + \lambda \|\beta\|^2, \quad (20)$$

where the regularizer $\lambda = 10^{-6}$ is introduced solely to avoid singular matrices. We also fit an intercept to accommodate targets with a non-zero mean. The analytical solution of problem 20 is

$$\beta_\theta = \arg \min_{\beta} \mathcal{L}_\theta(\beta) = (\mathbf{X}_{\text{train}} \mathbf{X}_{\text{train}}^T + \lambda \mathbf{I})^{-1} \mathbf{X}_{\text{train}} \mathbf{y}_{\theta, \text{train}}. \quad (21)$$

The performance of a network on a given task is quantified by the coefficient of determination of the read-out β_θ on the test set:

$$s_\theta = 1 - \frac{\|\mathbf{y}_{\theta, \text{test}} - \hat{\mathbf{y}}_{\theta, \text{test}}\|^2}{\|\mathbf{y}_{\theta, \text{test}} - \bar{\mathbf{y}}_{\theta, \text{test}}\|^2}, \quad (22)$$

where $\hat{\mathbf{y}}_\theta = \beta_\theta \mathbf{X}_{\text{test}}$ and $\bar{\mathbf{y}}_{\theta, \text{test}}$ denote the network’s prediction and the target mean, respectively. The scalar s_θ therefore quantifies the normalized mismatch between the prediction and the ground truth. A perfect match yields $s_\theta = 1$, $s_\theta = 0$ corresponds to chance-level performance (i.e., predicting only the target mean), and negative values indicate performance worse than chance (approaching $-\infty$ for infinitely poor predictions).

Because s_θ depends on the particular samples in the training and test subsets, we estimate its uncertainty by expanding the training set threefold and training three independent read-outs for each task (instead of a single one). An alternative would be to use bootstrapping, which would introduce overlapping. All scores reported in the main text are averaged over these three independent read-outs; the resulting standard deviations are extremely small (see Fig. S.17 and S.18).

4.6 Complexity and similarity definition

Task complexity is a network-independent measure that quantifies the non-triviality of the mapping from the input $\mathbf{u}(t)$ to the target output $y_\theta(t)$. Several absolute metrics could be used, e.g., mutual information between input and output, the Wasserstein distance, Jeffreys divergence, the degree of non-linearity (expressed via the multi-index of multivariate polynomials), or— for the analytical mappings considered here— the number of elementary operations required to transform $\mathbf{u}(t)$ into $y_\theta(t)$. For simplicity, however, we adopt a relative measure by comparing each task to the simplest task in our set. A natural choice for this reference task is the identity function

$$y_0(t) = u_k(t), \quad (23)$$

which simply relays the k -th component of the input without any modification. For a generic task $y_\theta(t) = u_k(t + \Delta)^d$, we define its complexity as the cosine dissimilarity to the reference:

$$C = 1 - \left| \frac{\mathbf{y}_\theta^T \cdot \mathbf{y}_0}{\|\mathbf{y}_\theta\| \|\mathbf{y}_0\|} \right|. \quad (24)$$

A perfect alignment with the reference yields $C = 0$, whereas tasks orthogonal to the reference achieve the maximal complexity $C = 1$.

Cosine similarity is also used to quantify the similarity between pairs of tasks (Fig. 2B and S.4B). Specifically, the similarity between tasks θ and θ' is defined as the cosine of the angle between their centered vectors:

$$S_{\theta\theta'} = \frac{(\mathbf{y}_\theta - \bar{\mathbf{y}}_\theta)^T \cdot (\mathbf{y}_{\theta'} - \bar{\mathbf{y}}_{\theta'})}{\|\mathbf{y}_\theta - \bar{\mathbf{y}}_\theta\| \|\mathbf{y}_{\theta'} - \bar{\mathbf{y}}_{\theta'}\|}. \quad (25)$$

Subtracting the mean eliminates static offsets, ensuring that tasks that are dynamically independent but share the same average are not mistakenly identified as similar.

4.7 Overlap and dimensionality definition

The temporal overlap between a network's state $\mathbf{X}(t)$ and a task $y_\theta(t)$ is computed in a similar way. First, we orthogonalize the state by applying principal-component analysis (PCA) to obtain $\hat{\mathbf{X}}(t)$, which captures 99.9% of the variance. Then, we evaluate the cosine similarity between the mean-subtracted task $y_\theta(t) - \bar{y}_\theta$ and each orthogonalized neuronal component $\hat{x}_i(t)$:

$$\cos \alpha_{\theta,i} = \frac{(\mathbf{y}_\theta - \bar{\mathbf{y}}_\theta)^T \cdot \hat{\mathbf{x}}_i}{\|\mathbf{y}_\theta - \bar{\mathbf{y}}_\theta\| \|\hat{\mathbf{x}}_i\|}. \quad (26)$$

Because the states are orthogonalized, the total overlap between task θ and the state $\mathbf{X}(t)$ is the sum of the squared partial overlaps:

$$\text{Overlap}(y_\theta(t), \mathbf{X}(t)) = \sum_{i=1}^N \cos^2 \alpha_{\theta,i}. \quad (27)$$

Note that this definition of overlap is closely related to the notion of *information processing capacity* (IPC) introduced in [108]. In short, IPC decomposes the state into orthonormal polynomials (e.g., Hermite, Legendre, Laguerre). The i -th decomposition coefficient—equivalent to the cosine similarity between the normalized state and the i -th basis function—determines the capacity of the state to perform the processing type specified by basis i . Because the polynomial bases are orthogonal by construction, IPC provides a complete quantification of a system's ability to carry out independent types of processing. While [108] proved that the IPC of any dynamical system is bounded by the number of its dynamical units, [109] showed that, when such systems are used to reconstruct a task, networks perform best when the IPC of the system and that of the task are maximally similar. In other words, reconstruction error is minimized when the network's state contains exactly the same processing required by the task. These studies rely on the existence of well-defined Hilbert spaces in which both the task and all neuronal states can be represented [110]. There are many ways to span a Hilbert space; IPC adopts the convenient basis that disentangles different processing types from one another. However, because performance in reservoir computers depends only on the quality of task reconstruction, it suffices to measure the extent to which the (incomplete) basis set formed by the neural states spans a given task. Forming a complete basis set—whether the IPC basis or any other—is unnecessary. Also note that, since we always add a constant term to our state $\mathbf{X}(t)$ during regression, the mean value of every task can always be captured. Consequently, the non-trivial overlap must be computed between the states and the mean-subtracted values of the task.

For dimensionality we use the participation ratio as a proxy because it is computationally simple and robust [111, 112]. Let the centered state be $\mathbf{X}_c(t) = \mathbf{X}(t) - \mathbb{E}[\mathbf{X}(t)]$, and denote its singular values by $\{\sigma_i\}$. The participation ratio is then defined as

$$d_{\text{PR}} = \frac{(\sum_i \sigma_i^2)^2}{\sum_i \sigma_i^4}, \quad (28)$$

where σ_i denotes the i -th singular value. For a system of N neurons recorded over $T > N$ time steps, d_{PR} is bounded between 1 (all variance concentrated in a single component) and N (all units contribute equally to the variance) [111, 113]. A higher participation ratio reflects less regular, more “jagged” neural trajectories. However, this irregularity is constrained by the regularities of the driving input [113] and by the dynamics of the system [111]. The low-dimensional neural states in Fig. 6C are therefore likely due to the Lorenzian input, whose fractal dimension is very close to 2 [114].

4.8 Emulation of network dynamics on neuromorphic hardware

We investigated energy efficiency using two state-of-the-art neuromorphic platforms, Loihi 2 and SpiNNaker 2. Loihi 2, developed by Intel Labs, implements networks of spiking neurons directly in hardware, enabling rapid processing of complex data while consuming very little energy [115–117]. In contrast, SpiNNaker 2, a neuromorphic computing platform developed by TU Dresden and the University of Manchester, achieves high efficiency and flexibility by running neural networks on asynchronously communicating general-purpose ARM processors [118–120]. Both systems exhibit exceptional energy efficiency—particularly for time-series processing tasks [115–117, 121–123]—and are therefore poised to contribute strongly to more sustainable high-performance computing as well as to edge-device computing.

To emulate the dynamics of our simulated networks on neuromorphic hardware, we first computed the mean firing rate of each neuron in the CPU-based simulations. Then, on both SpiNNaker 2 and Loihi 2, we instantiated networks with the same connectivity as in the corresponding CPU implementation and imposed the calculated mean firing rates ν_{set} on each neuron by applying a neuron-specific background input (cf. Eq. 10 and [124], p. 164):

$$v_{\text{bg}} = \frac{v_{\text{thr}}}{1 - \exp(-1/(\nu_{\text{set}} \cdot \tau_m))}, \quad (29)$$

where v_{thr} is an arbitrarily chosen firing threshold of 0.01 V and τ_m is a membrane time constant of 0.01 s. In addition, all synaptic weights—including those of existing connections—are set to zero. This common approach ensures that the full computational load associated with relaying spikes is accounted for [125], while spikes do not affect the imposed firing rates ν_{set} . Consequently, because neurons and synapses in the recurrent network perform exactly the same number of operations as they would in a complete simulation, we obtain fair estimates of runtime and energy consumption. Note that the specific choice of membrane time constants is irrelevant here, since the neuron-specific inputs already incorporate the effects of time-constant heterogeneity. On both Loihi 2 and SpiNNaker 2, we emulated the full range of network sizes N considered in the study.

4.9 Cost estimation

Since a network’s performance depends on its state $\mathbf{X}(t)$, we estimate the energy cost of generating those states. This cost, however, is hardware-dependent, so a distinct definition of cost is used for each implementation. Moreover, we separate the cost into a static (activity-independent) component and a dynamic (activity-specific) component. The total energy cost of the state is therefore the sum of its static and dynamic components. The definitions of these components for the different implementations are described in Supplementary Section A.

5 Other software resources

Throughout this work, we employed free and open-source libraries (apart from the proprietary components required for the neuromorphic hardware frameworks). The rate-based networks were implemented in Python using NumPy [126] and SciPy [127], and parallelized with Joblib [128]. The Brian simulator [129] was used for the CPU implementation of spiking networks. For visualization, we used Matplotlib [130] and Seaborn [131] (and, optionally, SciencePlots [132]).

To measure the energy and computational efficiency of the spiking model on neuromorphic hardware, we employed the following software packages: for SpiNNaker 2, `py-spinnaker2` (forked from commit 12c3828), `s2-sim2lab-app` (commit 4cd3a06), and `spinnaker2-stm` (commit b449cca); for Loihi 2, the Lava-Loihi package (release version 0.7.0).

6 Code availability

All scripts used for CPU simulations and neuromorphic emulations will be made publicly available upon acceptance.

7 Acknowledgements

We would like to thank Dr. Sebastian Schmitt, Dr. Andrew Lehr, Dr. Michael Fauth, Ms. Shirin Shafiee, and Ms. Nahid Safari for fruitful discussions. This research was funded by the German Research Foundation via project no. 536022519 and SFB1286, projects C01 and Z01, as well as by the German Federal Ministry of Education and Research (BMBF), grant no. 01IS22093A “KISSKI”.

References

- [1] J. W. Mink, R. J. Blumenshine, and D. B. Adams. “Ratio of Central Nervous System to Body Metabolism in Vertebrates: Its Constancy and Functional Basis”. In: *American Journal of Physiology-Regulatory, Integrative and Comparative Physiology* 241.3 (Sept. 1, 1981), R203–R212. ISSN: 0363-6119, 1522-1490. DOI: 10.1152/ajpregu.1981.241.3.R203. URL: <https://www.physiology.org/doi/10.1152/ajpregu.1981.241.3.R203>.
- [2] Chia-Chien Chen et al. “Morphological Heterogeneity of Layer VI Neurons in Mouse Barrel Cortex”. In: *Journal of Comparative Neurology* 512.6 (2009), pp. 726–746. ISSN: 1096-9861. DOI: 10.1002/cne.21926. URL: <https://onlinelibrary.wiley.com/doi/abs/10.1002/cne.21926>.
- [3] Hongkui Zeng and Joshua R. Sanes. “Neuronal Cell-Type Classification: Challenges, Opportunities and the Path Forward”. In: *Nat Rev Neurosci* 18.9 (Sept. 2017), pp. 530–546. ISSN: 1471-0048. DOI: 10.1038/nrn.2017.85. URL: <https://www.nature.com/articles/nrn.2017.85>.
- [4] Stephanie C Seeman et al. “Sparse Recurrent Excitatory Connectivity in the Microcircuit of the Adult Mouse and Human Cortex”. In: *eLife* 7 (Sept. 26, 2018). Ed. by Inna Slutsky, Eve Marder, and Per Jesper Sjöström, e37349. ISSN: 2050-084X. DOI: 10.7554/eLife.37349. URL: <https://doi.org/10.7554/eLife.37349>.
- [5] Mark S. Cembrowski and Nelson Spruston. “Heterogeneity within Classical Cell Types Is the Rule: Lessons from Hippocampal Pyramidal Neurons”. In: *Nat Rev Neurosci* 20.4 (Apr. 2019), pp. 193–204. ISSN: 1471-0048. DOI: 10.1038/s41583-019-0125-5. URL: <https://www.nature.com/articles/s41583-019-0125-5>.
- [6] J. Michael Hasse et al. “Morphological Heterogeneity among Corticogeniculate Neurons in Ferrets: Quantification and Comparison with a Previous Report in Macaque Monkeys”. In: *Journal of Comparative Neurology* 527.3 (2019), pp. 546–557. ISSN: 1096-9861. DOI: 10.1002/cne.24451. URL: <https://onlinelibrary.wiley.com/doi/abs/10.1002/cne.24451>.
- [7] Renchao Chen et al. “Decoding Molecular and Cellular Heterogeneity of Mouse Nucleus Accumbens”. In: *Nat Neurosci* 24.12 (Dec. 2021), pp. 1757–1771. ISSN: 1546-1726. DOI: 10.1038/s41593-021-00938-x. URL: <https://www.nature.com/articles/s41593-021-00938-x>.
- [8] Zizhen Yao et al. “A Taxonomy of Transcriptomic Cell Types across the Isocortex and Hippocampal Formation”. In: *Cell* 184.12 (June 10, 2021), 3222–3241.e26. ISSN: 0092-8674. DOI: 10.1016/j.cell.2021.04.021. URL: <https://www.sciencedirect.com/science/article/pii/S0092867421005018>.
- [9] Luke Campagnola et al. “Local Connectivity and Synaptic Dynamics in Mouse and Human Neocortex”. In: *Science* 375.6585 (Mar. 11, 2022), eabj5861. DOI: 10.1126/science.abj5861. URL: <https://www.science.org/doi/10.1126/science.abj5861>.
- [10] Zizhen Yao et al. “A High-Resolution Transcriptomic and Spatial Atlas of Cell Types in the Whole Mouse Brain”. In: *Nature* 624.7991 (Dec. 2023), pp. 317–332. ISSN: 1476-4687. DOI: 10.1038/s41586-023-06812-z. URL: <https://www.nature.com/articles/s41586-023-06812-z>.
- [11] Jonah Langlieb et al. “The Molecular Cytoarchitecture of the Adult Mouse Brain”. In: *Nature* 624.7991 (Dec. 2023), pp. 333–342. ISSN: 1476-4687. DOI: 10.1038/s41586-023-06818-7. URL: <https://www.nature.com/articles/s41586-023-06818-7>.
- [12] David Golomb and John Rinzel. “Dynamics of Globally Coupled Inhibitory Neurons with Heterogeneity”. In: *Phys. Rev. E* 48.6 (Dec. 1, 1993), pp. 4810–4814. DOI: 10.1103/PhysRevE.48.4810. URL: <https://link.aps.org/doi/10.1103/PhysRevE.48.4810>.
- [13] Maoz Shamir and Haim Sompolinsky. “Implications of Neuronal Diversity on Population Coding”. In: *Neural Computation* 18.8 (Aug. 1, 2006), pp. 1951–1986. ISSN: 0899-7667. DOI: 10.1162/neco.2006.18.8.1951. URL: <https://doi.org/10.1162/neco.2006.18.8.1951>.

- [14] Srdjan Ostojic, Nicolas Brunel, and Vincent Hakim. “Synchronization Properties of Networks of Electrically Coupled Neurons in the Presence of Noise and Heterogeneities”. In: *J Comput Neurosci* 26.3 (June 1, 2009), pp. 369–392. ISSN: 1573-6873. DOI: 10.1007/s10827-008-0117-3. URL: <https://doi.org/10.1007/s10827-008-0117-3>.
- [15] Toni Pérez et al. “The Constructive Role of Diversity in the Global Response of Coupled Neuron Systems”. In: *Philosophical Transactions of the Royal Society A: Mathematical, Physical and Engineering Sciences* 368.1933 (Dec. 28, 2010), pp. 5619–5632. DOI: 10.1098/rsta.2010.0264. URL: <https://royalsocietypublishing.org/doi/10.1098/rsta.2010.0264>.
- [16] Stefano Luccioli and Antonio Politi. “Irregular Collective Behavior of Heterogeneous Neural Networks”. In: *Phys. Rev. Lett.* 105.15 (Oct. 7, 2010), p. 158104. DOI: 10.1103/PhysRevLett.105.158104. URL: <https://link.aps.org/doi/10.1103/PhysRevLett.105.158104>.
- [17] Shreejoy J. Tripathy et al. “Intermediate Intrinsic Diversity Enhances Neural Population Coding”. In: *Proceedings of the National Academy of Sciences* 110.20 (May 14, 2013), pp. 8248–8253. DOI: 10.1073/pnas.1221214110. URL: <https://www.pnas.org/doi/full/10.1073/pnas.1221214110>.
- [18] Johannes Lengler, Florian Jug, and Angelika Steger. “Reliable Neuronal Systems: The Importance of Heterogeneity”. In: *PLOS ONE* 8.12 (Dec. 4, 2013), e80694. ISSN: 1932-6203. DOI: 10.1371/journal.pone.0080694. URL: <https://journals.plos.org/plosone/article?id=10.1371/journal.pone.0080694>.
- [19] Jorge F. Mejias and André Longtin. “Differential Effects of Excitatory and Inhibitory Heterogeneity on the Gain and Asynchronous State of Sparse Cortical Networks”. In: *Front. Comput. Neurosci.* 8 (Sept. 12, 2014). ISSN: 1662-5188. DOI: 10.3389/fncom.2014.00107. URL: <https://www.frontiersin.org/journals/computational-neuroscience/articles/10.3389/fncom.2014.00107/full>.
- [20] David Angulo-Garcia et al. “Death and Rebirth of Neural Activity in Sparse Inhibitory Networks”. In: *New J. Phys.* 19.5 (May 2017), p. 053011. ISSN: 1367-2630. DOI: 10.1088/1367-2630/aa69ff. URL: <https://dx.doi.org/10.1088/1367-2630/aa69ff>.
- [21] Manuel Beiran et al. “Coding of Time-Dependent Stimuli in Homogeneous and Heterogeneous Neural Populations”. In: *J Comput Neurosci* 44.2 (Apr. 1, 2018), pp. 189–202. ISSN: 1573-6873. DOI: 10.1007/s10827-017-0674-4. URL: <https://doi.org/10.1007/s10827-017-0674-4>.
- [22] Stefano Luccioli, David Angulo-Garcia, and Alessandro Torcini. “Neural Activity of Heterogeneous Inhibitory Spiking Networks with Delay”. In: *Phys. Rev. E* 99.5 (May 23, 2019), p. 052412. ISSN: 2470-0045, 2470-0053. DOI: 10.1103/PhysRevE.99.052412. URL: <https://link.aps.org/doi/10.1103/PhysRevE.99.052412>.
- [23] Matteo Di Volo and Alain Destexhe. “Optimal Responsiveness and Information Flow in Networks of Heterogeneous Neurons”. In: *Sci Rep* 11.1 (Sept. 2, 2021), p. 17611. ISSN: 2045-2322. DOI: 10.1038/s41598-021-96745-2. URL: <https://www.nature.com/articles/s41598-021-96745-2>.
- [24] Alain Destexhe. “Noise Enhancement of Neural Information Processing”. In: *Entropy* 24.12 (12 Dec. 2022), p. 1837. ISSN: 1099-4300. DOI: 10.3390/e24121837. URL: <https://www.mdpi.com/1099-4300/24/12/1837>.
- [25] Richard Gast, Sara A. Solla, and Ann Kennedy. “Neural Heterogeneity Controls Computations in Spiking Neural Networks”. In: *Proceedings of the National Academy of Sciences* 121.3 (Jan. 16, 2024), e2311885121. DOI: 10.1073/pnas.2311885121. URL: <https://www.pnas.org/doi/full/10.1073/pnas.2311885121>.
- [26] Krishnan Padmanabhan and Nathaniel N. Urban. “Intrinsic Biophysical Diversity Decorrelates Neuronal Firing While Increasing Information Content”. In: *Nat Neurosci* 13.10 (Oct. 2010), pp. 1276–1282. ISSN: 1546-1726. DOI: 10.1038/nn.2630. URL: <https://www.nature.com/articles/nn.2630>.
- [27] Lars A. Holmstrom et al. “Efficient Encoding of Vocalizations in the Auditory Midbrain”. In: *J Neurosci* 30.3 (Jan. 20, 2010), pp. 802–819. ISSN: 0270-6474. DOI: 10.1523/JNEUROSCI.1964-09.2010. PMID: 20089889. URL: <https://www.ncbi.nlm.nih.gov/pmc/articles/PMC6633079/>.
- [28] Kamilla Angelo et al. “A Biophysical Signature of Network Affiliation and Sensory Processing in Mitral Cells”. In: *Nature* 488.7411 (Aug. 2012), pp. 375–378. ISSN: 1476-4687. DOI: 10.1038/nature11291. URL: <https://www.nature.com/articles/nature11291>.
- [29] Ann Kennedy et al. “A Temporal Basis for Predicting the Sensory Consequences of Motor Commands in an Electric Fish”. In: *Nat Neurosci* 17.3 (Mar. 2014), pp. 416–422. ISSN: 1546-1726. DOI: 10.1038/nn.3650. URL: <https://www.nature.com/articles/nn.3650>.
- [30] Chris I. De Zeeuw et al. “Heterogeneous Encoding of Temporal Stimuli in the Cerebellar Cortex”. In: *Nat Commun* 14.1 (Nov. 21, 2023), p. 7581. ISSN: 2041-1723. DOI: 10.1038/s41467-023-43139-9. URL: <https://www.nature.com/articles/s41467-023-43139-9>.

- [31] Takashi Matsubara. “Conduction Delay Learning Model for Unsupervised and Supervised Classification of Spatio-Temporal Spike Patterns”. In: *Front. Comput. Neurosci.* 11 (Nov. 21, 2017). ISSN: 1662-5188. DOI: 10.3389/fncom.2017.00104. URL: <https://www.frontiersin.org/journals/computational-neuroscience/articles/10.3389/fncom.2017.00104/full>.
- [32] Wei Fang et al. *Incorporating Learnable Membrane Time Constant to Enhance Learning of Spiking Neural Networks*. Aug. 16, 2021. arXiv: 2007.05785 [cs]. URL: <http://arxiv.org/abs/2007.05785>. Pre-published.
- [33] Nicolas Perez-Nieves et al. “Neural Heterogeneity Promotes Robust Learning”. In: *Nat Commun* 12.1 (Oct. 4, 2021), p. 5791. ISSN: 2041-1723. DOI: 10.1038/s41467-021-26022-3. URL: <https://www.nature.com/articles/s41467-021-26022-3>.
- [34] Chloe N. Winston et al. “Heterogeneity in Neuronal Dynamics Is Learned by Gradient Descent for Temporal Processing Tasks”. In: *Neural Comput* 35.4 (2023), pp. 555–592. ISSN: 0899-7667. DOI: 10.1162/neco_a_01571. PMID: 36827598. URL: <https://www.ncbi.nlm.nih.gov/pmc/articles/PMC10044000/>.
- [35] Hanle Zheng et al. “Temporal Dendritic Heterogeneity Incorporated with Spiking Neural Networks for Learning Multi-Timescale Dynamics”. In: *Nat Commun* 15.1 (Jan. 4, 2024), p. 277. ISSN: 2041-1723. DOI: 10.1038/s41467-023-44614-z. URL: <https://www.nature.com/articles/s41467-023-44614-z>.
- [36] Timothy P. Lillicrap et al. “Backpropagation and the Brain”. In: *Nat Rev Neurosci* 21.6 (June 2020), pp. 335–346. ISSN: 1471-0048. DOI: 10.1038/s41583-020-0277-3. URL: <https://www.nature.com/articles/s41583-020-0277-3>.
- [37] Alexander Ororbia et al. *A Review of Neuroscience-Inspired Machine Learning*. Feb. 16, 2024. DOI: 10.48550/arXiv.2403.18929. arXiv: 2403.18929 [cs]. URL: <http://arxiv.org/abs/2403.18929>. Pre-published.
- [38] Robert M. French. “Catastrophic Forgetting in Connectionist Networks”. In: *Trends in Cognitive Sciences* 3.4 (Apr. 1, 1999), pp. 128–135. ISSN: 1364-6613, 1879-307X. DOI: 10.1016/S1364-6613(99)01294-2. PMID: 10322466. URL: [https://www.cell.com/trends/cognitive-sciences/abstract/S1364-6613\(99\)01294-2](https://www.cell.com/trends/cognitive-sciences/abstract/S1364-6613(99)01294-2).
- [39] Everton L. Aleixo et al. *Catastrophic Forgetting in Deep Learning: A Comprehensive Taxonomy*. Dec. 16, 2023. DOI: 10.48550/arXiv.2312.10549. arXiv: 2312.10549 [cs]. URL: <http://arxiv.org/abs/2312.10549>. Pre-published.
- [40] Jerry L Chen and Elly Nedivi. “Neuronal Structural Remodeling: Is It All about Access?” In: *Current Opinion in Neurobiology*. Neuronal and Glial Cell Biology – New Technologies 20.5 (Oct. 1, 2010), pp. 557–562. ISSN: 0959-4388. DOI: 10.1016/j.comb.2010.06.002. URL: <https://www.sciencedirect.com/science/article/pii/S0959438810000991>.
- [41] Ennio Pannese. “Morphological Changes in Nerve Cells during Normal Aging”. In: *Brain Struct Funct* 216.2 (June 1, 2011), pp. 85–89. ISSN: 1863-2661. DOI: 10.1007/s00429-011-0308-y. URL: <https://doi.org/10.1007/s00429-011-0308-y>.
- [42] A. Mehonic and A. J. Kenyon. “Brain-Inspired Computing Needs a Master Plan”. In: *Nature* 604.7905 (Apr. 2022), pp. 255–260. ISSN: 1476-4687. DOI: 10.1038/s41586-021-04362-w. URL: <https://www.nature.com/articles/s41586-021-04362-w>.
- [43] Joel Hestness et al. *Deep Learning Scaling Is Predictable, Empirically*. Dec. 1, 2017. DOI: 10.48550/arXiv.1712.00409. arXiv: 1712.00409 [cs]. URL: <http://arxiv.org/abs/1712.00409>. Pre-published.
- [44] Yang Liu et al. *Datasets for Large Language Models: A Comprehensive Survey*. Feb. 28, 2024. DOI: 10.48550/arXiv.2402.18041. arXiv: 2402.18041 [cs]. URL: <http://arxiv.org/abs/2402.18041>. Pre-published.
- [45] Herbert Jaeger. “Adaptive Nonlinear System Identification with Echo State Networks”. In: *Advances in Neural Information Processing Systems*. Vol. 15. MIT Press, 2002. URL: <https://proceedings.neurips.cc/paper/2002/hash/426f990b332ef8193a61cc90516c1245-Abstract.html>.
- [46] Nils Bertschinger and Thomas Natschläger. “Real-Time Computation at the Edge of Chaos in Recurrent Neural Networks”. In: *Neural Computation* 16.7 (July 1, 2004), pp. 1413–1436. ISSN: 0899-7667, 1530-888X. DOI: 10.1162/089976604323057443. URL: <https://direct.mit.edu/neco/article/16/7/1413-1436/6890>.
- [47] Mantas Lukoševičius and Herbert Jaeger. “Reservoir Computing Approaches to Recurrent Neural Network Training”. In: *Computer Science Review* 3.3 (Aug. 1, 2009), pp. 127–149. ISSN: 1574-0137. DOI: 10.1016/j.cosrev.2009.03.005. URL: <https://www.sciencedirect.com/science/article/pii/S1574013709000173>.

- [48] Gouhei Tanaka et al. “Reservoir Computing with Diverse Timescales for Prediction of Multiscale Dynamics”. In: *Phys. Rev. Res.* 4.3 (July 28, 2022), p. L032014. DOI: 10.1103/PhysRevResearch.4.L032014. URL: <https://link.aps.org/doi/10.1103/PhysRevResearch.4.L032014>.
- [49] Arash Golmohammadi and Christian Tetzlaff. *Robust Computation with Intrinsic Heterogeneity*. Dec. 6, 2024. DOI: 10.48550/arXiv.2412.05126. arXiv: 2412.05126 [cs]. URL: <http://arxiv.org/abs/2412.05126>. Pre-published.
- [50] Anirudh Goyal and Yoshua Bengio. “Inductive Biases for Deep Learning of Higher-Level Cognition”. In: *Proceedings of the Royal Society A: Mathematical, Physical and Engineering Sciences* 478.2266 (Oct. 12, 2022), p. 20210068. DOI: 10.1098/rspa.2021.0068. URL: <https://royalsocietypublishing.org/doi/full/10.1098/rspa.2021.0068>.
- [51] Edward N. Lorenz. “Deterministic Nonperiodic Flow”. In: *Journal of the Atmospheric Sciences* 20.2 (Mar. 1, 1963), pp. 130–141. ISSN: 0022-4928, 1520-0469. DOI: 10.1175/1520-0469(1963)020<0130:DNF>2.0.CO;2. URL: https://journals.ametsoc.org/view/journals/atmsc/20/2/1520-0469_1963_020_0130_dnf_2_0_co_2.xml.
- [52] William Gilpin. *Chaos as an Interpretable Benchmark for Forecasting and Data-Driven Modelling*. Jan. 29, 2023. DOI: 10.48550/arXiv.2110.05266. arXiv: 2110.05266 [cs]. URL: <http://arxiv.org/abs/2110.05266>. Pre-published.
- [53] Wolfgang Maass, Thomas Natschläger, and Henry Markram. “Real-Time Computing Without Stable States: A New Framework for Neural Computation Based on Perturbations”. In: *Neural Computation* 14.11 (Nov. 1, 2002), pp. 2531–2560. ISSN: 0899-7667, 1530-888X. DOI: 10.1162/089976602760407955. URL: <https://direct.mit.edu/neco/article/14/11/2531-2560/6650>.
- [54] Lyudmila Grigoryeva and Juan-Pablo Ortega. “Echo State Networks Are Universal”. In: *Neural Networks* 108 (Dec. 1, 2018), pp. 495–508. ISSN: 0893-6080. DOI: 10.1016/j.neunet.2018.08.025. URL: <https://www.sciencedirect.com/science/article/pii/S089360801830251X>.
- [55] Lukas Gonon, Lyudmila Grigoryeva, and Juan-Pablo Ortega. *Approximation Bounds for Random Neural Networks and Reservoir Systems*. Feb. 16, 2021. DOI: 10.48550/arXiv.2002.05933. arXiv: 2002.05933 [cs, eess, math]. URL: <http://arxiv.org/abs/2002.05933>. Pre-published.
- [56] S. Boyd and L. Chua. “Fading Memory and the Problem of Approximating Nonlinear Operators with Volterra Series”. In: *IEEE Trans. Circuits Syst.* 32.11 (Nov. 1985), pp. 1150–1161. ISSN: 0098-4094. DOI: 10.1109/TCS.1985.1085649. URL: <http://ieeexplore.ieee.org/document/1085649/>.
- [57] Herbert Jaeger. “The “Echo State” Approach to Analysing and Training Recurrent Neural Networks-with an Erratum Note”. In: *Bonn, Germany: German National Research Center for Information Technology GMD Technical Report* 148 (Jan. 1, 2001).
- [58] Francesco Bullo. *Contraction Theory for Dynamical Systems*. 1.1. Kindle Direct Publishing, 2024. ISBN: 979-8-8366-4680-6. URL: <https://fbullo.github.io/ctds>.
- [59] Steven H. Strogatz. *Nonlinear Dynamics and Chaos: With Applications to Physics, Biology, Chemistry, and Engineering*. Second edition. Boulder, CO: Westview Press, a member of the Perseus Books Group, 2015. 513 pp. ISBN: 978-0-8133-4910-7.
- [60] H. Sompolinsky, A. Crisanti, and H. J. Sommers. “Chaos in Random Neural Networks”. In: *Phys. Rev. Lett.* 61.3 (July 18, 1988), pp. 259–262. DOI: 10.1103/PhysRevLett.61.259. URL: <https://link.aps.org/doi/10.1103/PhysRevLett.61.259>.
- [61] Guangyu Robert Yang and Xiao-Jing Wang. “Artificial Neural Networks for Neuroscientists: A Primer”. In: *Neuron* 107.6 (Sept. 23, 2020), pp. 1048–1070. ISSN: 0896-6273. DOI: 10.1016/j.neuron.2020.09.005. PMID: 32970997. URL: [https://www.cell.com/neuron/abstract/S0896-6273\(20\)30705-4](https://www.cell.com/neuron/abstract/S0896-6273(20)30705-4).
- [62] Biswa Sengupta et al. “The Effect of Cell Size and Channel Density on Neuronal Information Encoding and Energy Efficiency”. In: *J Cereb Blood Flow Metab* 33.9 (Sept. 1, 2013), pp. 1465–1473. ISSN: 0271-678X. DOI: 10.1038/jcbfm.2013.103. URL: <https://doi.org/10.1038/jcbfm.2013.103>.
- [63] Jeremy E Niven. “Neuronal Energy Consumption: Biophysics, Efficiency and Evolution”. In: *Current Opinion in Neurobiology*. Microcircuit Computation and Evolution 41 (Dec. 1, 2016), pp. 129–135. ISSN: 0959-4388. DOI: 10.1016/j.conb.2016.09.004. URL: <https://www.sciencedirect.com/science/article/pii/S0959438816301210>.
- [64] Karim G. Habashy et al. “Adapting to Time: Why Nature May Have Evolved a Diverse Set of Neurons”. In: *PLOS Computational Biology* 20.12 (Dec. 13, 2024), e1012673. ISSN: 1553-7358. DOI: 10.1371/journal.pcbi.1012673. URL: <https://journals.plos.org/ploscompbiol/article?id=10.1371/journal.pcbi.1012673>.

- [65] German I. Parisi et al. “Continual Lifelong Learning with Neural Networks: A Review”. In: *Neural Networks* 113 (May 1, 2019), pp. 54–71. ISSN: 0893-6080. DOI: 10.1016/j.neunet.2019.01.012. URL: <https://www.sciencedirect.com/science/article/pii/S0893608019300231>.
- [66] Yoshua Bengio et al. *Towards Biologically Plausible Deep Learning*. Aug. 9, 2016. DOI: 10.48550/arXiv.1502.04156. arXiv: 1502.04156 [cs]. URL: <http://arxiv.org/abs/1502.04156>. Pre-published.
- [67] James C. R. Whittington and Rafal Bogacz. “Theories of Error Back-Propagation in the Brain”. In: *Trends in Cognitive Sciences* 23.3 (Mar. 1, 2019), pp. 235–250. ISSN: 1364-6613, 1879-307X. DOI: 10.1016/j.tics.2018.12.005. PMID: 30704969. URL: [https://www.cell.com/trends/cognitive-sciences/abstract/S1364-6613\(19\)30012-9](https://www.cell.com/trends/cognitive-sciences/abstract/S1364-6613(19)30012-9).
- [68] Blake A. Richards and Timothy P. Lillicrap. “Dendritic Solutions to the Credit Assignment Problem”. In: *Curr Opin Neurobiol* 54 (Feb. 2019), pp. 28–36. ISSN: 1873-6882. DOI: 10.1016/j.conb.2018.08.003. PMID: 30205266.
- [69] Mufeng Tang, Yibo Yang, and Yali Amit. “Biologically Plausible Training Mechanisms for Self-Supervised Learning in Deep Networks”. In: *Front. Comput. Neurosci.* 16 (Mar. 21, 2022). ISSN: 1662-5188. DOI: 10.3389/fncom.2022.789253. URL: <https://www.frontiersin.org/journals/computational-neuroscience/articles/10.3389/fncom.2022.789253/full>.
- [70] Navid Shervani-Tabar and Robert Rosenbaum. “Meta-Learning Biologically Plausible Plasticity Rules with Random Feedback Pathways”. In: *Nat Commun* 14.1 (Mar. 31, 2023), p. 1805. ISSN: 2041-1723. DOI: 10.1038/s41467-023-37562-1. URL: <https://www.nature.com/articles/s41467-023-37562-1>.
- [71] Yoshua Bengio, Yann Lecun, and Geoffrey Hinton. “Deep Learning for AI”. In: *Commun. ACM* 64.7 (July 2021), pp. 58–65. ISSN: 0001-0782, 1557-7317. DOI: 10.1145/3448250. URL: <https://dl.acm.org/doi/10.1145/3448250>.
- [72] Ian J. Goodfellow et al. *Maxout Networks*. Sept. 20, 2013. DOI: 10.48550/arXiv.1302.4389. arXiv: 1302.4389 [stat]. URL: <http://arxiv.org/abs/1302.4389>. Pre-published.
- [73] David Eigen, Marc’Aurelio Ranzato, and Ilya Sutskever. *Learning Factored Representations in a Deep Mixture of Experts*. Mar. 9, 2014. DOI: 10.48550/arXiv.1312.4314. arXiv: 1312.4314 [cs]. URL: <http://arxiv.org/abs/1312.4314>. Pre-published.
- [74] Wei Wang et al. “Volatile Resistive Switching Memory Based on Ag Ion Drift/Diffusion—Part II: Compact Modeling”. In: *IEEE Transactions on Electron Devices* 66.9 (Sept. 2019), pp. 3802–3808. ISSN: 1557-9646. DOI: 10.1109/TED.2019.2928888. URL: <https://ieeexplore.ieee.org/abstract/document/8788455>.
- [75] Erika Covi et al. “Switching Dynamics of Ag-Based Filamentary Volatile Resistive Switching Devices—Part I: Experimental Characterization”. In: *IEEE Trans. Electron Devices* 68.9 (Sept. 2021), pp. 4335–4341. ISSN: 0018-9383, 1557-9646. DOI: 10.1109/TED.2021.3076029. URL: <https://ieeexplore.ieee.org/document/9494108/>.
- [76] Sebastian Billaudelle et al. *An Accurate and Flexible Analog Emulation of AdEx Neuron Dynamics in Silicon*. Sept. 19, 2022. DOI: 10.48550/arXiv.2209.09280. arXiv: 2209.09280 [cs]. URL: <http://arxiv.org/abs/2209.09280>. Pre-published.
- [77] Ronald E. Crochiere and Lawrence R. Rabiner. *Multirate Digital Signal Processing*. Prentice-Hall, 1983. 440 pp. ISBN: 978-0-13-605162-6. Google Books: X_NSAAAAAMAAJ.
- [78] Anjana Santhosh and Rishikesh Narayanan. *Diversity in the Impact of Heterogeneities on Recurrent Networks Performing a Cognitive Task*. Jan. 20, 2025. DOI: 10.1101/2025.01.20.633872. URL: <http://biorxiv.org/lookup/doi/10.1101/2025.01.20.633872>. Pre-published.
- [79] Allen Institute for Brain Science. *Synaptic Physiology - Intralaminar Connectivity and Synaptic Dynamics*. 2019. URL: <https://brain-map.org/our-research/connectivity/synaptic-physiology>.
- [80] Pengfei Sun et al. “Learnable Axonal Delay in Spiking Neural Networks Improves Spoken Word Recognition”. In: *Front. Neurosci.* 17 (Nov. 9, 2023). ISSN: 1662-453X. DOI: 10.3389/fnins.2023.1275944. URL: <https://www.frontiersin.org/journals/neuroscience/articles/10.3389/fnins.2023.1275944/full>.
- [81] Stefan J. Kiebel, Jean Daunizeau, and Karl J. Friston. “A Hierarchy of Time-Scales and the Brain”. In: *PLoS Computational Biology* 4.11 (Nov. 14, 2008), e1000209. ISSN: 1553-7358. DOI: 10.1371/journal.pcbi.1000209. URL: <https://journals.plos.org/ploscompbiol/article?id=10.1371/journal.pcbi.1000209>.
- [82] Sean E. Cavanagh, Laurence T. Hunt, and Steven W. Kennerley. “A Diversity of Intrinsic Timescales Underlie Neural Computations”. In: *Front. Neural Circuits* 14 (Dec. 21, 2020). ISSN: 1662-5110. DOI: 10.3389/fncir.2020.615626. URL: <https://www.frontiersin.org/journals/neural-circuits/articles/10.3389/fncir.2020.615626/full>.

- [83] D. H. Hubel and T. N. Wiesel. “Receptive Fields, Binocular Interaction and Functional Architecture in the Cat’s Visual Cortex”. In: *The Journal of Physiology* 160.1 (Jan. 1962), pp. 106–154. ISSN: 0022-3751, 1469-7793. DOI: 10.1113/jphysiol.1962.sp006837. URL: <https://physoc.onlinelibrary.wiley.com/doi/10.1113/jphysiol.1962.sp006837>.
- [84] D. H. Hubel and T. N. Wiesel. “Receptive Fields and Functional Architecture of Monkey Striate Cortex”. In: *The Journal of Physiology* 195.1 (1968), pp. 215–243. ISSN: 1469-7793. DOI: 10.1113/jphysiol.1968.sp008455. URL: <https://onlinelibrary.wiley.com/doi/abs/10.1113/jphysiol.1968.sp008455>.
- [85] Jean-Pierre Rospars et al. “Heterogeneity and Convergence of Olfactory First-Order Neurons Account for the High Speed and Sensitivity of Second-Order Neurons”. In: *PLoS Computational Biology* 10.12 (Dec. 4, 2014), e1003975. ISSN: 1553-7358. DOI: 10.1371/journal.pcbi.1003975. URL: <https://journals.plos.org/ploscompbiol/article?id=10.1371/journal.pcbi.1003975>.
- [86] Saltanat Ualiyeva et al. “A Nasal Cell Atlas Reveals Heterogeneity of Tuft Cells and Their Role in Directing Olfactory Stem Cell Proliferation”. In: *Sci Immunol* 9.92 (Feb. 2, 2024), eabq4341. ISSN: 2470-9468. DOI: 10.1126/sciimmunol.abq4341. PMID: 38306414. URL: <https://www.ncbi.nlm.nih.gov/pmc/articles/PMC11127180/>.
- [87] Sidney P. Kuo, Laura A. Bradley, and Laurence O. Trussell. “Heterogeneous Kinetics and Pharmacology of Synaptic Inhibition in the Chick Auditory Brainstem”. In: *J. Neurosci.* 29.30 (July 29, 2009), pp. 9625–9634. ISSN: 0270-6474, 1529-2401. DOI: 10.1523/JNEUROSCI.0103-09.2009. PMID: 19641125. URL: <https://www.jneurosci.org/content/29/30/9625>.
- [88] Patrick O. Kanold, Israel Nelken, and Daniel B. Polley. “Local versus Global Scales of Organization in Auditory Cortex”. In: *Trends in Neurosciences* 37.9 (Sept. 1, 2014), pp. 502–510. ISSN: 0166-2236. DOI: 10.1016/j.tins.2014.06.003. URL: <https://www.sciencedirect.com/science/article/pii/S0166223614001003>.
- [89] Sebastian A. Vasquez-Lopez et al. “Thalamic Input to Auditory Cortex Is Locally Heterogeneous but Globally Tonotopic”. In: *Elife* 6 (Sept. 11, 2017), e25141. ISSN: 2050-084X. DOI: 10.7554/eLife.25141. PMID: 28891466.
- [90] Can Tao et al. “Diversity in Excitation-Inhibition Mismatch Underlies Local Functional Heterogeneity in the Rat Auditory Cortex”. In: *Cell Reports* 19.3 (Apr. 18, 2017), pp. 521–531. ISSN: 2211-1247. DOI: 10.1016/j.celrep.2017.03.061. URL: <https://www.sciencedirect.com/science/article/pii/S2211124717304229>.
- [91] Graziana Gatto et al. “Neuronal Diversity in the Somatosensory System: Bridging the Gap between Cell Type and Function”. In: *Current Opinion in Neurobiology*. Neuronal Identity 56 (June 1, 2019), pp. 167–174. ISSN: 0959-4388. DOI: 10.1016/j.conb.2019.03.002. URL: <https://www.sciencedirect.com/science/article/pii/S0959438819300017>.
- [92] Ziteng Han et al. “Investigating the Heterogeneity within the Somatosensory-Motor Network and Its Relationship with the Attention and Default Systems”. In: *PNAS Nexus* 2.9 (Sept. 1, 2023), pgad276. ISSN: 2752-6542. DOI: 10.1093/pnasnexus/pgad276. URL: <https://doi.org/10.1093/pnasnexus/pgad276>.
- [93] William T Redman et al. “Robust Variability of Grid Cell Properties within Individual Grid Modules Enhances Encoding of Local Space”. In: *eLife* 13 (Feb. 20, 2025). Ed. by Adrien Peyrache and Panayiota Poirazi, RP100652. ISSN: 2050-084X. DOI: 10.7554/eLife.100652. URL: <https://doi.org/10.7554/eLife.100652>.
- [94] Nagham Khouri-Farah et al. “FOXP Genes Regulate Purkinje Cell Diversity and Cerebellar Morphogenesis”. In: *Nat Neurosci* 28.10 (Oct. 2025), pp. 2022–2033. ISSN: 1546-1726. DOI: 10.1038/s41593-025-02042-w. URL: <https://www.nature.com/articles/s41593-025-02042-w>.
- [95] Thomas L. Griffiths et al. “Probabilistic Models of Cognition: Exploring Representations and Inductive Biases”. In: *Trends in Cognitive Sciences* 14.8 (Aug. 1, 2010), pp. 357–364. ISSN: 1364-6613, 1879-307X. DOI: 10.1016/j.tics.2010.05.004. PMID: 20576465. URL: [https://www.cell.com/trends/cognitive-sciences/abstract/S1364-6613\(10\)00112-9](https://www.cell.com/trends/cognitive-sciences/abstract/S1364-6613(10)00112-9).
- [96] C. van Vreeswijk and H. Sompolinsky. “Chaos in Neuronal Networks with Balanced Excitatory and Inhibitory Activity”. In: *Science* (Dec. 6, 1996). URL: <https://www.science.org/doi/abs/10.1126/science.274.5293.1724>.
- [97] Nicolas Brunel. “Dynamics of Sparsely Connected Networks of Excitatory and Inhibitory Spiking Neurons”. In: *J Comput Neurosci* 8.3 (May 1, 2000), pp. 183–208. ISSN: 1573-6873. DOI: 10.1023/A:1008925309027. URL: <https://doi.org/10.1023/A:1008925309027>.

- [98] Kanaka Rajan and L. F. Abbott. “Eigenvalue Spectra of Random Matrices for Neural Networks”. In: *Phys. Rev. Lett.* 97.18 (Nov. 2, 2006), p. 188104. DOI: 10.1103/PhysRevLett.97.188104. URL: <https://link.aps.org/doi/10.1103/PhysRevLett.97.188104>.
- [99] Yashar Ahmadian and Kenneth D. Miller. “What Is the Dynamical Regime of Cerebral Cortex?” In: *Neuron* 109.21 (Nov. 2021), pp. 3373–3391. ISSN: 08966273. DOI: 10.1016/j.neuron.2021.07.031. URL: <https://linkinghub.elsevier.com/retrieve/pii/S0896627321005754>.
- [100] Sophie Denève and Christian K. Machens. “Efficient Codes and Balanced Networks”. In: *Nat Neurosci* 19.3 (Mar. 2016), pp. 375–382. ISSN: 1097-6256, 1546-1726. DOI: 10.1038/nn.4243. URL: <http://www.nature.com/articles/nn.4243>.
- [101] C. Van Vreeswijk and H. Sompolinsky. “Chaotic Balanced State in a Model of Cortical Circuits”. In: *Neural Computation* 10.6 (Aug. 1, 1998), pp. 1321–1371. ISSN: 0899-7667, 1530-888X. DOI: 10.1162/089976698300017214. URL: <https://direct.mit.edu/neco/article/10/6/1321-1371/6179>.
- [102] Michael C. Mackey and Leon Glass. “Oscillation and Chaos in Physiological Control Systems”. In: *Science* 197.4300 (July 15, 1977), pp. 287–289. DOI: 10.1126/science.267326. URL: <https://www.science.org/doi/10.1126/science.267326>.
- [103] Hendrik Wernecke, Bulcsú Sándor, and Claudius Gros. “Chaos in Time Delay Systems, an Educational Review”. In: *Physics Reports* 824 (Sept. 2019), pp. 1–40. ISSN: 03701573. DOI: 10.1016/j.physrep.2019.08.001. arXiv: 1901.04826 [nlin]. URL: <http://arxiv.org/abs/1901.04826>.
- [104] A.F. Atiya and A.G. Parlos. “New Results on Recurrent Network Training: Unifying the Algorithms and Accelerating Convergence”. In: *IEEE Transactions on Neural Networks* 11.3 (May 2000), pp. 697–709. ISSN: 1941-0093. DOI: 10.1109/72.846741. URL: <https://ieeexplore.ieee.org/document/846741/>.
- [105] Cédric Gernigon et al. “Low-Precision Floating-Point for Efficient On-Board Deep Neural Network Processing”. In: *2023 European Data Handling & Data Processing Conference (EDHPC)*. 2023 European Data Handling & Data Processing Conference (EDHPC). Oct. 2023, pp. 1–8. DOI: 10.23919/EDHPC59100.2023.10396014. URL: <https://ieeexplore.ieee.org/document/10396014>.
- [106] Naigang Wang et al. *Training Deep Neural Networks with 8-Bit Floating Point Numbers*. Dec. 19, 2018. DOI: 10.48550/arXiv.1812.08011. arXiv: 1812.08011 [cs]. URL: <http://arxiv.org/abs/1812.08011>. Pre-published.
- [107] Marcus K. Benna and Stefano Fusi. “Computational Principles of Synaptic Memory Consolidation”. In: *Nat Neurosci* 19.12 (Dec. 2016), pp. 1697–1706. ISSN: 1546-1726. DOI: 10.1038/nn.4401. URL: <https://www.nature.com/articles/nn.4401>.
- [108] Joni Dambre et al. “Information Processing Capacity of Dynamical Systems”. In: *Sci Rep* 2.1 (1 July 19, 2012), p. 514. ISSN: 2045-2322. DOI: 10.1038/srep00514. URL: <https://www.nature.com/articles/srep00514>.
- [109] Tomoyuki Kubota, Hirokazu Takahashi, and Kohei Nakajima. “Unifying Framework for Information Processing in Stochastically Driven Dynamical Systems”. In: *Phys. Rev. Research* 3.4 (Nov. 23, 2021), p. 043135. ISSN: 2643-1564. DOI: 10.1103/PhysRevResearch.3.043135. URL: <https://link.aps.org/doi/10.1103/PhysRevResearch.3.043135>.
- [110] O. P. Le Maître and Omar M. Knio. *Spectral Methods for Uncertainty Quantification: With Applications to Computational Fluid Dynamics*. Scientific Computation. Dordrecht: Springer Netherlands, 2010. ISBN: 978-90-481-3519-6 978-90-481-3520-2. DOI: 10.1007/978-90-481-3520-2. URL: <https://link.springer.com/10.1007/978-90-481-3520-2>.
- [111] Lianli Gao et al. “Learning in High-Dimensional Multimedia Data: The State of the Art”. In: *Multimedia Systems* 23.3 (June 1, 2017), pp. 303–313. ISSN: 1432-1882. DOI: 10.1007/s00530-015-0494-1. URL: <https://doi.org/10.1007/s00530-015-0494-1>.
- [112] Stefano Recanatesi et al. *A Scale-Dependent Measure of System Dimensionality*. Dec. 21, 2020. DOI: 10.1101/2020.12.19.423618.
- [113] Carsen Stringer et al. “High-Dimensional Geometry of Population Responses in Visual Cortex”. In: *Nature* 571.7765 (July 2019), pp. 361–365. ISSN: 1476-4687. DOI: 10.1038/s41586-019-1346-5. URL: <https://www.nature.com/articles/s41586-019-1346-5>.
- [114] N. V. Kuznetsov et al. “The Lorenz System: Hidden Boundary of Practical Stability and the Lyapunov Dimension”. In: *Nonlinear Dyn* 102.2 (Oct. 1, 2020), pp. 713–732. ISSN: 1573-269X. DOI: 10.1007/s11071-020-05856-4. URL: <https://doi.org/10.1007/s11071-020-05856-4>.
- [115] Mike Davies et al. “Advancing Neuromorphic Computing With Loihi: A Survey of Results and Outlook”. In: *Proceedings of the IEEE* 109.5 (May 2021), pp. 911–934. ISSN: 1558-2256. DOI: 10.1109/JPROC.2021.3067593.

- [116] Sumit Bam Shrestha et al. “Efficient Video and Audio Processing with Loihi 2”. In: *ICASSP 2024 - 2024 IEEE International Conference on Acoustics, Speech and Signal Processing (ICASSP)*. ICASSP 2024 - 2024 IEEE International Conference on Acoustics, Speech and Signal Processing (ICASSP). Apr. 2024, pp. 13481–13485. DOI: 10.1109/ICASSP48485.2024.10448003. URL: <https://ieeexplore.ieee.org/document/10448003/>.
- [117] Alessandro Pierro et al. *Accelerating Linear Recurrent Neural Networks for the Edge with Unstructured Sparsity*. Aug. 13, 2025. DOI: 10.48550/arXiv.2502.01330. arXiv: 2502.01330 [cs]. URL: <http://arxiv.org/abs/2502.01330>. Pre-published.
- [118] Sebastian Höppner et al. *The SpiNNaker 2 Processing Element Architecture for Hybrid Digital Neuromorphic Computing*. Aug. 15, 2022. arXiv: 2103.08392 [cs]. URL: <http://arxiv.org/abs/2103.08392>. Pre-published.
- [119] Khaleelulla Khan Nazeer et al. *Language Modeling on a SpiNNaker 2 Neuromorphic Chip*. Jan. 24, 2024. DOI: 10.48550/arXiv.2312.09084. arXiv: 2312.09084 [cs]. URL: <http://arxiv.org/abs/2312.09084>. Pre-published.
- [120] Zihao Chen et al. “ON-OFF Neuromorphic ISING Machines Using Fowler-Nordheim Annealers”. In: *Nat Commun* 16.1 (Mar. 31, 2025), p. 3086. ISSN: 2041-1723. DOI: 10.1038/s41467-025-58231-5. URL: <https://www.nature.com/articles/s41467-025-58231-5>.
- [121] Yexin Yan et al. “Comparing Loihi with a SpiNNaker 2 Prototype on Low-Latency Keyword Spotting and Adaptive Robotic Control”. In: *Neuromorph. Comput.* 1.1 (July 2021), p. 014002. ISSN: 2634-4386. DOI: 10.1088/2634-4386/abf150. URL: <https://doi.org/10.1088/2634-4386/abf150>.
- [122] Bernhard Vogginger et al. *Neuromorphic Hardware for Sustainable AI Data Centers*. June 26, 2024. DOI: 10.48550/arXiv.2402.02521. arXiv: 2402.02521 [cs]. URL: <http://arxiv.org/abs/2402.02521>. Pre-published.
- [123] Narges Lux et al. “HPC-AI Benchmarks - A Comparative Overview of High-Performance Computing Hardware and AI Benchmarks across Domains”. In: *Journal of Artificial Intelligence* (2024). URL: <https://joaiar.org/articles/AIR-1017.html>.
- [124] Peter Dayan and L. F. Abbott. *Theoretical Neuroscience: Computational and Mathematical Modeling of Neural Systems*. Computational Neuroscience. Cambridge, Mass: Massachusetts Institute of Technology Press, 2001. 460 pp. ISBN: 978-0-262-04199-7.
- [125] Jannik Luboeinski et al. *Plastic Arbor: A Modern Simulation Framework for Synaptic Plasticity – from Single Synapses to Networks of Morphological Neurons*. Sept. 15, 2025. DOI: 10.48550/arXiv.2411.16445. arXiv: 2411.16445 [cs]. URL: <http://arxiv.org/abs/2411.16445>. Pre-published.
- [126] Charles R. Harris et al. “Array Programming with NumPy”. In: *Nature* 585.7825 (7825 Sept. 2020), pp. 357–362. ISSN: 1476-4687. DOI: 10.1038/s41586-020-2649-2. URL: <https://www.nature.com/articles/s41586-020-2649-2>.
- [127] Pauli Virtanen et al. “SciPy 1.0: Fundamental Algorithms for Scientific Computing in Python”. In: *Nat Methods* 17.3 (3 Mar. 2020), pp. 261–272. ISSN: 1548-7105. DOI: 10.1038/s41592-019-0686-2. URL: <https://www.nature.com/articles/s41592-019-0686-2>.
- [128] The joblib developers. *Joblib*. Version latest. Aug. 10, 2025. DOI: 10.5281/zenodo.14915601. URL: <https://github.com/joblib/joblib>.
- [129] Marcel Stimberg, Romain Brette, and Dan FM Goodman. “Brian 2, an Intuitive and Efficient Neural Simulator”. In: *eLife* 8 (Aug. 20, 2019), e47314. ISSN: 2050-084X. DOI: 10.7554/eLife.47314. URL: <https://elifesciences.org/articles/47314>.
- [130] John D. Hunter. “Matplotlib: A 2D Graphics Environment”. In: *Computing in Science & Engineering* 9.3 (May 2007), pp. 90–95. ISSN: 1558-366X. DOI: 10.1109/MCSE.2007.55.
- [131] Michael L. Waskom. “Seaborn: Statistical Data Visualization”. In: *Journal of Open Source Software* 6.60 (Apr. 6, 2021), p. 3021. ISSN: 2475-9066. DOI: 10.21105/joss.03021. URL: <https://joss.theoj.org/papers/10.21105/joss.03021>.
- [132] John Garrett et al. *Garrettj403/SciencePlots: 2.1.1*. Version 2.1.1. Zenodo, Nov. 25, 2023. DOI: 10.5281/zenodo.10206719. URL: <https://zenodo.org/records/10206719>.
- [133] David Attwell and Simon B. Laughlin. “An Energy Budget for Signaling in the Grey Matter of the Brain”. In: *J Cereb Blood Flow Metab* 21.10 (Oct. 2001), pp. 1133–1145. ISSN: 0271-678X, 1559-7016. DOI: 10.1097/00004647-200110000-00001. URL: <https://journals.sagepub.com/doi/10.1097/00004647-200110000-00001>.

- [134] Clare Howarth, Pdraig Gleeson, and David Attwell. “Updated Energy Budgets for Neural Computation in the Neocortex and Cerebellum”. In: *J Cereb Blood Flow Metab* 32.7 (July 1, 2012), pp. 1222–1232. ISSN: 0271-678X. DOI: 10.1038/jcbfm.2012.35. URL: <https://doi.org/10.1038/jcbfm.2012.35>.
- [135] Biswa Sengupta et al. “Action Potential Energy Efficiency Varies Among Neuron Types in Vertebrates and Invertebrates”. In: *PLoS computational biology* 6 (July 1, 2010), e1000840. DOI: 10.1371/journal.pcbi.1000840.
- [136] Christopher S. von Bartheld, Jami Bahney, and Suzanaerculano-Houzel. “The Search for True Numbers of Neurons and Glial Cells in the Human Brain: A Review of 150 Years of Cell Counting”. In: *Journal of Comparative Neurology* 524.18 (2016), pp. 3865–3895. ISSN: 1096-9861. DOI: 10.1002/cne.24040. URL: <https://onlinelibrary.wiley.com/doi/abs/10.1002/cne.24040>.
- [137] Christoph Ostrau et al. “Benchmarking Neuromorphic Hardware and Its Energy Expenditure”. In: *Front. Neurosci.* 16 (June 2, 2022). ISSN: 1662-453X. DOI: 10.3389/fnins.2022.873935. URL: <https://www.frontiersin.org/journals/neuroscience/articles/10.3389/fnins.2022.873935/full>.
- [138] Jason Yik et al. “The Neurobench Framework for Benchmarking Neuromorphic Computing Algorithms and Systems”. In: *Nat Commun* 16.1 (Feb. 11, 2025), p. 1545. ISSN: 2041-1723. DOI: 10.1038/s41467-025-56739-4. URL: <https://www.nature.com/articles/s41467-025-56739-4>.
- [139] *SpiNNaker2 STM Python Interface*. URL: <https://spinnaker2-stm-c5f3e7.gitlab.io/>.
- [140] *Lava-Nc/Lava*. Lava, Nov. 1, 2025. URL: <https://github.com/lava-nc/lava>.
- [141] Stefano Fusi, Earl K Miller, and Mattia Rigotti. “Why Neurons Mix: High Dimensionality for Higher Cognition”. In: *Current Opinion in Neurobiology*. Neurobiology of Cognitive Behavior 37 (Apr. 1, 2016), pp. 66–74. ISSN: 0959-4388. DOI: 10.1016/j.conb.2016.01.010. URL: <https://www.sciencedirect.com/science/article/pii/S0959438816000118>.
- [142] David Badre et al. “The Dimensionality of Neural Representations for Control”. In: *Current Opinion in Behavioral Sciences*. Computational Cognitive Neuroscience 38 (Apr. 1, 2021), pp. 20–28. ISSN: 2352-1546. DOI: 10.1016/j.cobeha.2020.07.002. URL: <https://www.sciencedirect.com/science/article/pii/S2352154620301042>.

A Cost estimation details

A.1 Rate implementation

In the rate-based networks, neuronal and synaptic activity is represented by numbers with a given floating-point precision (e.g., 32- or 64-bit). Consequently, generating the network state requires manipulating and storing these numbers throughout the simulation. We therefore define the total number of floating-point operations (FLOP) and the memory footprint (MEM) as the primary contributors to the overall cost. These quantities correspond to the dynamic and static costs, respectively.

Following the notation introduced in Section 4.1, a network with N neurons, N^2p recurrent synapses, and KN feed-forward synapses that receives a K -dimensional stimulus has costs that scale as follows:

$$E_{\text{mem}} = \underbrace{\mathcal{O}(N)}_{\text{state}} + \underbrace{\mathcal{O}(K)}_{\text{input}} + \underbrace{\mathcal{O}(N^2p)}_{\text{rec. weights}} + \underbrace{\mathcal{O}(NK)}_{\text{ff. weights}} + \underbrace{\mathcal{O}(1)}_{\text{shared time constants}} \quad (\text{homogeneous}) \quad (\text{S.1})$$

$$E_{\text{mem}} = \underbrace{\mathcal{O}(N)}_{\text{state}} + \underbrace{\mathcal{O}(K)}_{\text{input}} + \underbrace{\mathcal{O}(N^2p)}_{\text{rec. weights}} + \underbrace{\mathcal{O}(NK)}_{\text{ff. weights}} + \underbrace{\mathcal{O}(N)}_{\text{distinct time constants}} \quad (\text{heterogeneous}) \quad (\text{S.2})$$

$$E_{\text{flop}} = \underbrace{L}_{\text{timesteps}} \left(\underbrace{\mathcal{O}(N)}_{\text{volt. update}} + \underbrace{\mathcal{O}(N^2p)}_{\text{sum. rec. input}} + \underbrace{\mathcal{O}(NK)}_{\text{sum. ff. input}} \right) \quad (\text{homog. or heterog.}) \quad (\text{S.3})$$

Note that, although heterogeneous networks incur a slightly larger memory cost, the FLOP cost is identical for homogeneous and heterogeneous networks. Moreover, while E_{flop} scales with the number of timesteps L , the memory footprint E_{mem} does not depend on L , because the allocated memory remains constant throughout the simulation. The total number of timesteps is set to $L = L_{\text{train}} + L_{\text{test}}$, as defined in Section 4.5. Since L is scaled with the network size N , smaller networks are additionally less costly due to their shorter simulation time.

A.2 Spiking implementation

For our spiking networks, we estimated the metabolic cost of an equivalent biological network in terms of the total consumption of adenosine triphosphate (ATP) molecules. This enables us to quantify the benefit of heterogeneity in real neural tissue. Our estimates follow the framework of [133, 134], which partitions the total neuronal energy budget into signaling and housekeeping components. The signaling cost itself is further decomposed into five categories:

1. **Resting.** Even at rest neurons consume energy to maintain their membrane reversal potentials. This is achieved by the Na^+/K^+ pump, which continuously extrudes three Na^+ ions and imports two K^+ ions; each exchange consumes one ATP molecule. Using the Na^+ and K^+ currents at the resting potential together with the ionic charge, the total rate of ion exchange can be estimated. ATP is consumed by both neuronal and glial cells. The estimated consumption rates are
 - Neuron: $102 \text{ M ATP s}^{-1} \text{ cell}^{-1}$
 - Glia: $342 \text{ M ATP s}^{-1} \text{ cell}^{-1}$
2. **Action-potential generation and propagation.** To generate an action potential (AP) the membrane voltage must increase by roughly 50–100 mV (depending on the neuronal compartment). Given the specific membrane capacitance and the volume of the different compartments (axon, dendrite, and soma), one can compute the net positive charge that must be injected to produce such a voltage change. However, at any instant both positive and negative currents flow across the membrane. Consequently, the actual number of ions exchanged depends on the kinetics of the channels, specifically the overlap between Na^+ and K^+ currents. In the cerebral cortex, this overlap increases the total ion exchange by about 24% (according to [134], which updated the previously over-estimated value used in [133]) compared with an idealized AP with no overlap [135]. The resulting ATP usage per compartment is
 - Unmyelinated segments: $97.5 \text{ M ATP AP}^{-1}$
 - Cell body: $5.1 \text{ M ATP AP}^{-1}$
 - Dendrites: $16.2 \text{ M ATP AP}^{-1}$
3. **Presynaptic.** A presynaptic AP raises intracellular Ca^{2+} concentration, which must be restored by Na^+ exchange. The elevated Ca^{2+} also triggers vesicle processing and recycling (docking, fusion, exo- and endocytosis), which consumes ATP, albeit far less than the processes above. The estimated ATP cost per vesicle is
 - Ca^{2+} influx resetting: $12 \text{ k ATP vesicle}^{-1}$
 - Presynaptic vesicle recycling: 400 ATP AP^{-1}
4. **Postsynaptic.** Neurotransmitter release opens postsynaptic receptors for a finite time, allowing excess Na^+ ions to enter the postsynaptic neuron; these ions must be removed by the Na^+/K^+ pump. Different receptor types admit different amounts of Na^+ because of their distinct abundance and electrophysiological properties. The best available estimates, which take the relative abundance of receptors into account, give the following costs
 - non-NMDA: $67 \text{ k ATP vesicle}^{-1}$ (average)

- NMDA: 70 k ATP vesicle⁻¹
- mGlu: 3 k ATP vesicle⁻¹

5. **Glutamate recycling.** Glutamate molecules that are not taken up by postsynaptic receptors diffuse in the extracellular matrix and are recycled by glial cells. The ATP cost for glutamate uptake (by glia), intracellular processing, export to the neuron, and repackaging into a vesicle is approximately 1.1×10^4 ATP per glutamate molecule.

[133, 134] estimate that, on average, each vesicle contains about 4000 glutamate molecules. Combining the contributions above, the total ATP-consumption rate of a network with N neurons, N_{glia} glial cells, and $N^2 p$ synapses that fire at an average rate ν with neurotransmitter-release probability r is

$$\dot{E}(N, p, \nu, J, N_{\text{glia}}, r) = [(102 \times 10^6 \frac{\text{ATP}/s}{\text{glia}})N_{\text{glia}} + (342 \times 10^6 \frac{\text{ATP}/s}{\text{neuron}})N] \quad (\text{resting}) \quad (\text{S.4})$$

$$+ [(120 \times 10^6 \frac{\text{ATP}}{\text{spike}})N\nu] \quad (\text{AP gen. and prop.}) \quad (\text{S.5})$$

$$+ [(12.4 \times 10^3 \frac{\text{ATP}}{\text{release}})N^2 p \nu r] \sqrt{J} \quad (\text{presynaptic}) \quad (\text{S.6})$$

$$+ [(140 \times 10^3 \frac{\text{ATP}}{\text{release}})N^2 p \nu r] \sqrt{J} \quad (\text{postsynaptic}) \quad (\text{S.7})$$

$$+ [(11 \times 10^3 \frac{\text{ATP}}{\text{release}})N^2 p \nu r] \sqrt{J} \quad (\text{glutamate recycling}). \quad (\text{S.8})$$

In the formula above we assumed that the synaptic strength J modulates the pre- and post-synaptic terms equally. In our calculations we set $N_{\text{glia}} = N$ (cf. [136]) and $r = 1$ because all synapses in the simulations were deterministic, although Attwell and Laughlin [133] use the more realistic fusion probability $r = 0.25$ (2000 out of 8000 boutons release neurotransmitter). The firing rate ν is replaced by the temporal average measured in the simulation. Finally, the expression is multiplied by the total simulation time $T = L\Delta t$ to obtain the signaling energy.

In addition to the signaling energy, the housekeeping cost—comprising the subcellular machinery and cellular homeostasis—contributes to the total ATP expenditure. It is estimated that housekeeping accounts for an additional one-third of the total signaling-related energy [133, 134].

Since the housekeeping energy scales with activity, the total dynamic energy cost of the biological networks is taken as $\frac{4}{3}$ of the sum of Equations S.4–S.8, whereas the activity-independent energy expenditure corresponds only to Equation S.4.

A.3 Neuromorphic implementation

We measured both the total execution time and total energy consumption of the workload (cf. 4.8) on each neuromorphic board—each board provided by the manufacturer and containing a single SpiNNaker 2 or Loihi 2 chip—and repeated the measurements over ten trials. To separate static (constant-overhead) from dynamic (workload-related) energy costs, we first measured the total energy consumption of idle networks by simulating stimulus-free networks with the same neurons and synapses that never fire. This baseline energy reflects the hardware-related consumption and was taken as the static cost. Next, we emulated our spiking networks using the background input described in Section 4.8 for the same duration, measured the total energy again, and subtracted the idle energy for each network to estimate the activity-dependent dynamic power consumption.

Note that, because logging power measurements on both chips slowed the simulation, networks were simulated for only 100 timesteps. To enable a consistent comparison with the other implementations, both static and dynamic energy values were upsampled by a factor of $L/100$, where L is the intended number of timesteps for each network. We emphasize that we did not aim to develop an architecture-independent energy model; rather, we employed an energy-estimation strategy tailored to our tasks and network configurations. For a more thorough investigation of neuromorphic energy consumption, platform-wide benchmarks such as those in [137, 138] can be employed.

For power analysis of the SpiNNaker and Loihi chips, we used the SpiNNaker2 STM Python Interface [139] and Intel’s Lava [140] frameworks, both publicly available. Access to the chips, however, requires direct communication with the respective manufacturers.

B SNN to RNN conversion

To match the dynamics of rate- and spike-based neurons, we must ensure that the input–output (i.e., current–rate) relationship of the two models is comparable. An LIF neuron receiving a constant background input $I > \frac{v_{\text{thr}} - v_{\text{reset}}}{R}$ possesses a maximally normalized equilibrium firing rate given by

$$r_s(I) = \nu/\nu_{\text{max}} = \frac{1}{1 + \frac{\tau_m}{\tau_{\text{ref}}} \log\left(\frac{RI - (v_{\text{reset}} - E)}{RI - (v_{\text{thr}} - E)}\right)}, \quad (\text{S.9})$$

where the parameters are those introduced in Section 4.3. This expression is the generic form of Eq. 29. Similarly, for a rate neuron with the activation function defined in Eq. 9, the (normalized) firing rate at equilibrium—i.e., when $v(t) = I(t)R$ —is

$$r_r(I) = \frac{1}{1 + \exp(-IR)}. \quad (\text{S.10})$$

B.1 Global or local match

Assuming a fixed membrane time constant and refractory period, matching the dynamics corresponds to finding a set of parameters $(E, v_{\text{reset}}, v_{\text{thr}})$ that yields $r_s \approx r_r$ for all values of I , i.e.,

$$\min_{\{E, v_{\text{thr}}, v_{\text{reset}}\}} \mathcal{L} = ||r_r(I) - r_s(I)||^2. \quad (\text{S.11})$$

Figure S.1 shows the firing-rate curves of both models and their difference as a function of the input current. The minimization problem above yields a globally optimal solution. However, because the spiking neuron’s firing rate converges logarithmically to the asymptotic line $r = 1$, this global optimization places excessive weight on reducing the discrepancy at high- I values. In practice, I is bounded, so the problem should be solved over the (application-dependent) domain of I rather than over the entire real line.

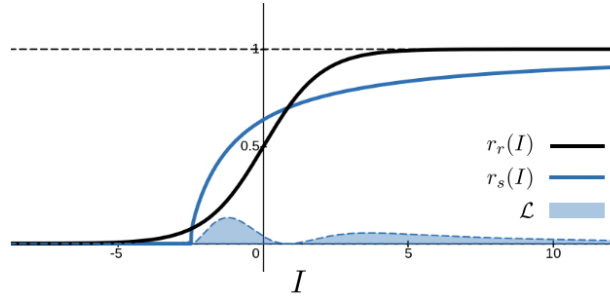


Figure S.1: Matching a spiking neuron to its rate-based counterpart. Normalized firing rates of the spiking neuron (blue) and the rate neuron (black) are shown together with their difference, $\mathcal{L}(I)$, as a function of the input current I . The LIF neuron parameters are set to $\tau_{\text{ref}} = 2$ ms, $\tau_m = 10$ ms, $R = 1 \Omega$, $v_{\text{thr}} - E = 2.8$ mV, and $v_{\text{reset}} - E = 2.5$ mV. \mathcal{L} is multiplied by two in the plot to highlight the slow convergence at large I values.

Note that if the membrane time constants are heterogeneous, solving the optimization problem S.11 yields neurons with heterogeneous thresholds, reversal potentials, and reset potentials.

B.2 Matching the mean activity

One can aim to match the baseline resting activity of the two neurons. This imposes the condition $r_s(0) = 0.5$, which, together with Eq. S.9, yields the following relationship among the reset potential, the threshold, and the reversal potential:

$$v_{\text{reset}} - E = (v_{\text{thr}} - E) \exp(\tau_{\text{ref}}/\tau_m) \quad (\text{S.12})$$

This condition can be combined with the global or local optimization problem above to further constrain the other parameters.

C Distinction between task–state overlap and dimensionality

Expanding dimensionality has long been known to improve performance on both classification and regression tasks [53, 141, 142], but performance improvements due to heterogeneity are not always accompanied by an expansion of dimensionality. To understand why, we must clarify what constitutes higher performance in temporal tasks.

Consider the following simple example: the activity of neurons in a network, $x_i(t)$, is linearly read out to reconstruct a periodic function $y(t)$ composed of two sinusoids (Fig. S.2A). The most efficient way to represent such a task perfectly is to use two independent and specialized units, $x_1(t)$ and $x_2(t)$, that oscillate at exactly the same frequencies. If such units exist, then, with respect to $y(t)$, the activity of the remaining neurons is entirely irrelevant. Consequently, a two-dimensional system that generates activity patterns $x_1(t)$ and $x_2(t)$ performs as well as a high-dimensional system that also contains other independent activity patterns (Fig. S.2B). Conversely, a network’s activity may be high-dimensional yet insufficient for this simple task if none of its neurons’ states overlap with the sinusoids in $y(t)$ (Fig. S.2C). This counterexample shows that higher dimensionality is beneficial only when the extra dimensions span, overlap, or align with the temporal modes required by the tasks.

Simply put, an ideal network is one whose neuronal spectra have peaks that align well with those of the tasks.

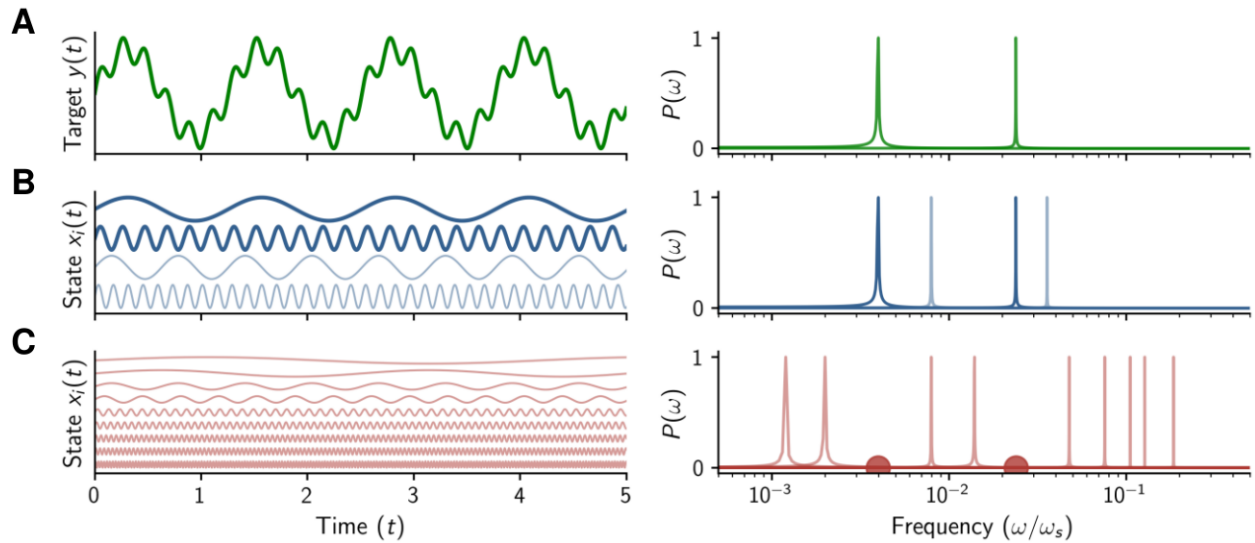


Figure S.2: High performance requires better state–task alignment. (A) Temporal (right) and frequency (left) representations of a simple target function composed of two sinusoids. This target is to be reconstructed linearly by two candidate networks. (B) The first network consists of four independent neurons, two of which oscillate at frequencies that match those of the target function (bold lines). Consequently, a linear combination of the network’s state can perfectly reconstruct the target. (C) The second network contains many more neurons but lacks units with the frequencies required by the target function (marked with red circles). Despite its higher dimensionality than the first network, it fails to reconstruct the simple task.

D Other timeseries

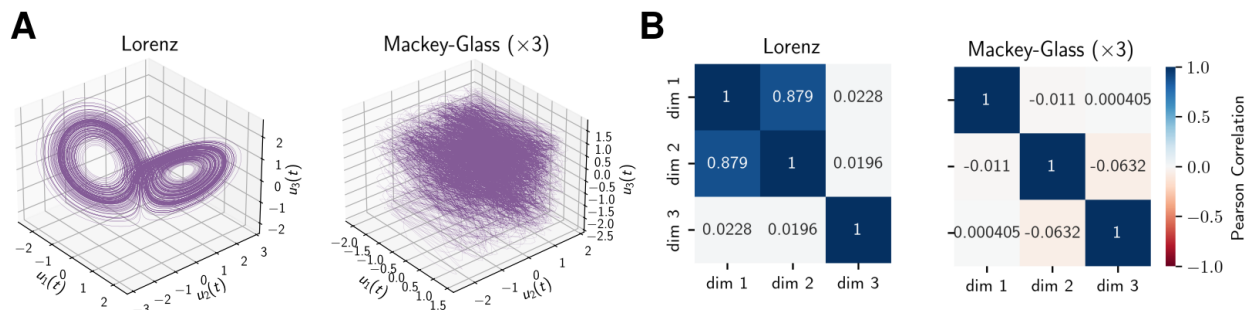


Figure S.3: Construction of multidimensional time series without an attractor (A) The attractor (left) is completely eliminated when the input consists of three independent Mackey-Glass time series with delay parameters 10, 50, and 80 (right). (B) Pearson correlation between the input components shows that joint information is removed when three Mackey-Glass trajectories are used.

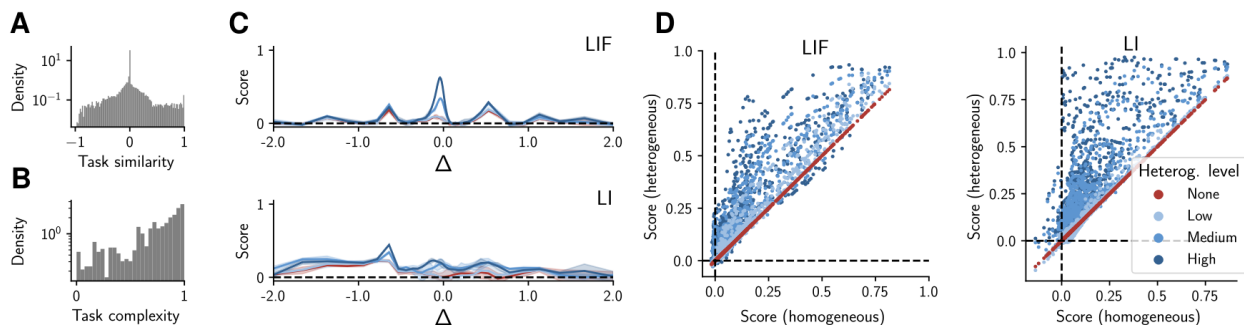


Figure S.4: Heterogeneity improves processing of chaotic time series without an attractor. As in Figure 2, but here the input consists of three Mackey-Glass processes with delay parameters 10, 50, and 80. While the first component is periodic, the other two are chaotic. (A,B) The tasks generated by this input are independent and span different complexity levels. (C–D) Despite the lack of an attractor, heterogeneity enhances performance across all tasks. Panel (C) illustrates how the networks approximate the square of the time-shifted third (chaotic) component. The barely visible shaded areas in (C) represent the standard deviation, enlarged fivefold, across three independent trials.

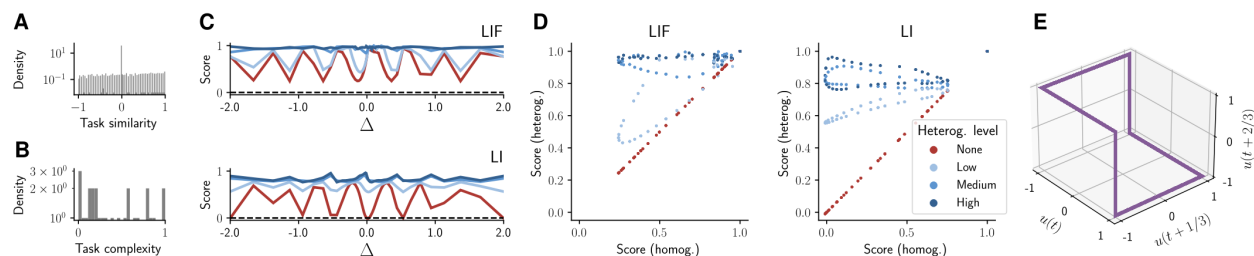


Figure S.5: Demonstration of a relatively simple task. As in Fig. S.4, but using the stimulus $u(t) = |\sin(t)|$. The tasks are constructed as before with the family \mathcal{F}_θ . Because the stimulus is periodic, it is considerably simpler than the chaotic inputs. Nevertheless, the fixed value and the abrupt change at each half-cycle make the tasks non-trivial for temporal networks with fading memory. In all cases, heterogeneous networks achieve better performance.

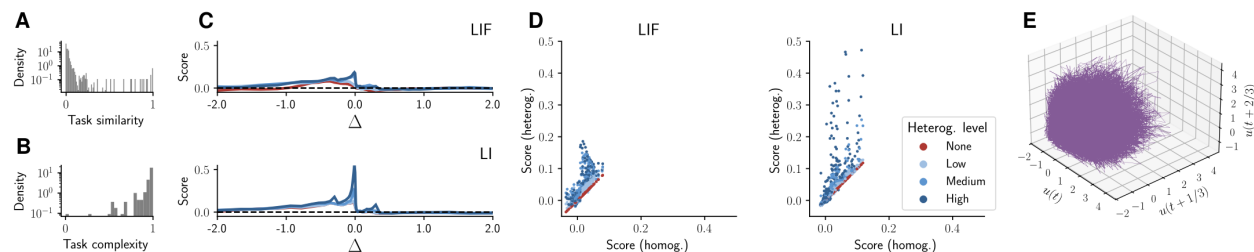


Figure S.6: Demonstration for an overly complicated task. As in Fig. S.4, but using the nonlinear autoregressive moving-average (NARMA) time series of order 30 as the stimulus. NARMA is a chaotic one-dimensional time series. As before, all heterogeneous networks outperform the homogeneous ones.

E Extended robustness figures

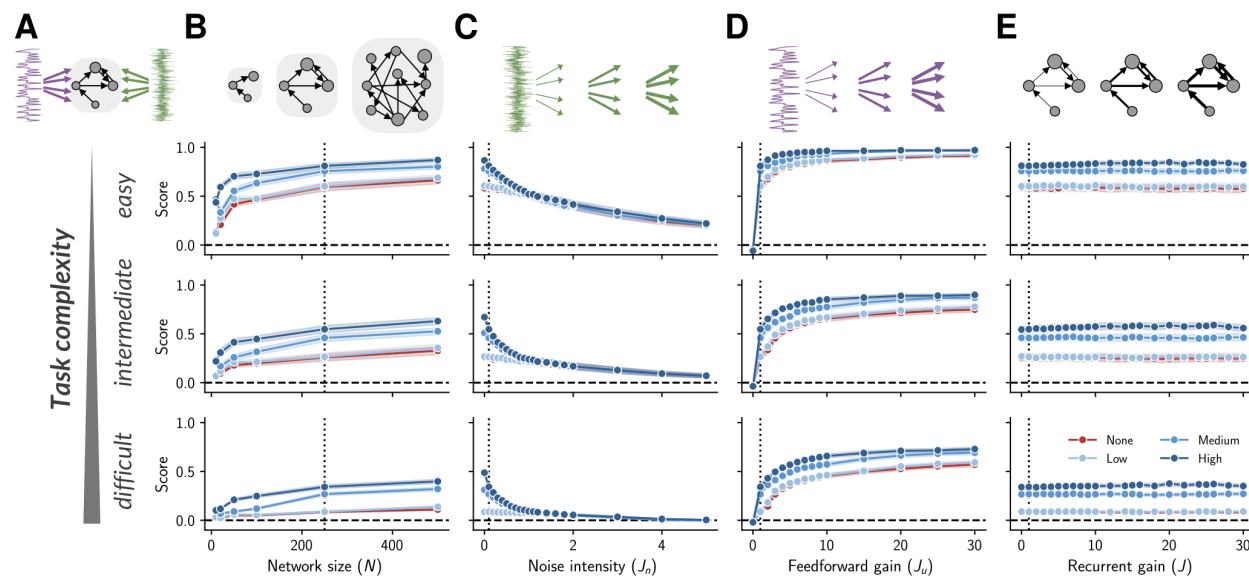


Figure S.7: Neuronal heterogeneity renders networks robust. As in Fig. 3, but for networks of LIF neurons. The shaded area indicates the 95% confidence interval across tasks within the corresponding complexity tier. Unlike rate-based networks, the scores do not drop to the chance-level value in panel (E) because LIF networks remain in a non-chaotic regime, operating at firing rates far below their maximum. See Fig. S.20G.

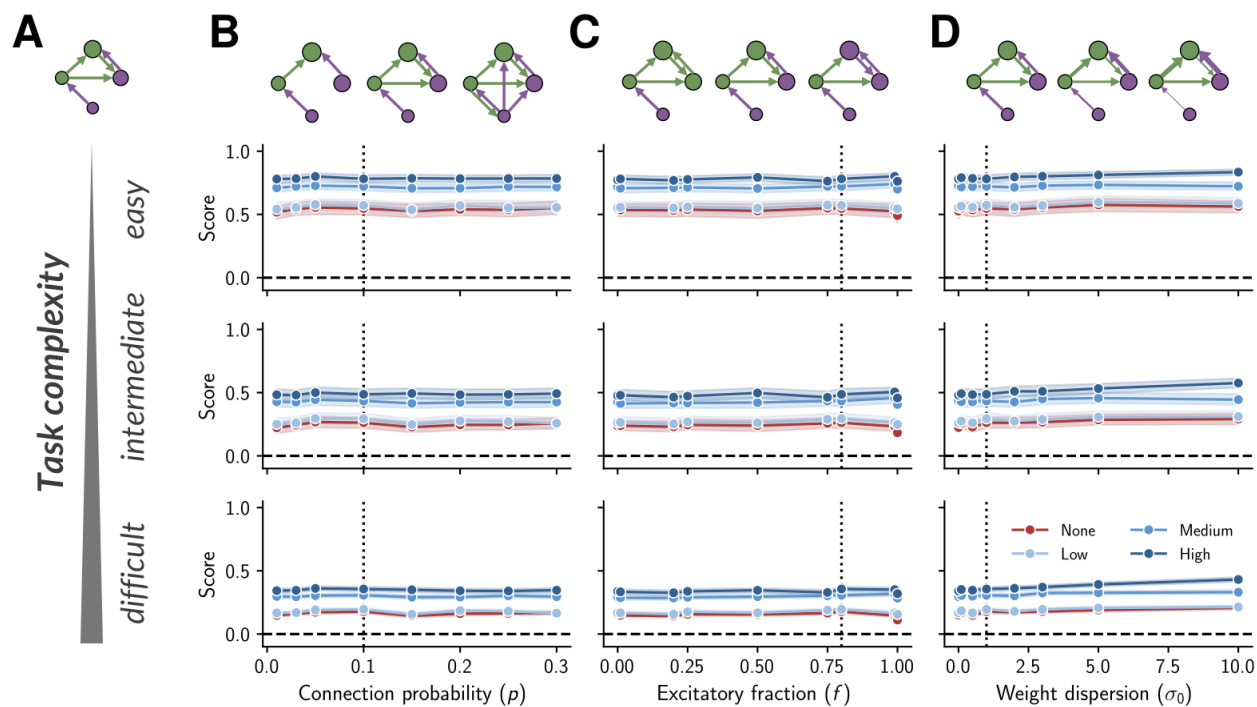


Figure S.8: Effect of population size and synaptic weights. (A) (Top) Schematic of the recurrent connections in the networks. (Bottom) Task-complexity tiers. (B–D) (Top) Schematic of the varied hyperparameter: connection probability (B), fraction of excitatory neurons (C), and weight dispersion (D), which controls the degree to which Dale’s law is respected. (Bottom) When excitatory–inhibitory balance is preserved, none of these changes affect the performance of rate-based networks at any level of heterogeneity. The shaded areas in all panels indicate the 95% confidence interval across tasks within the corresponding complexity tier.

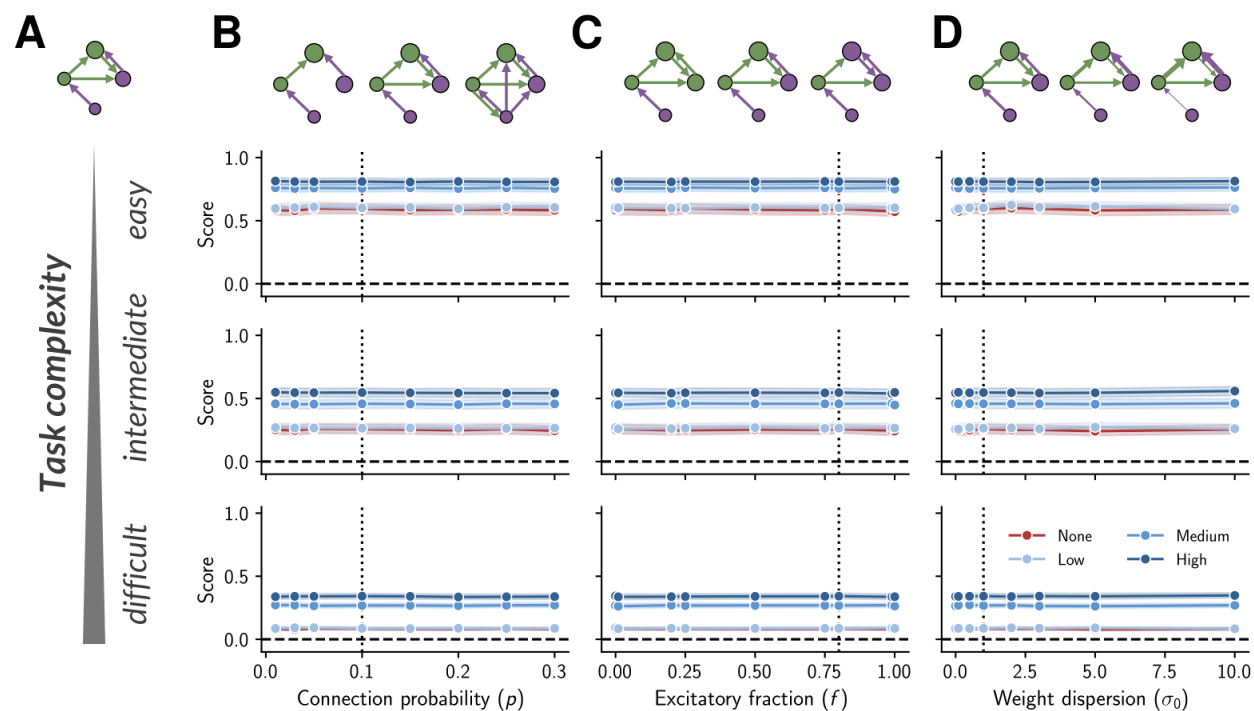


Figure S.9: Effect of population and weights. Same as Fig. S.8, but for spiking networks.

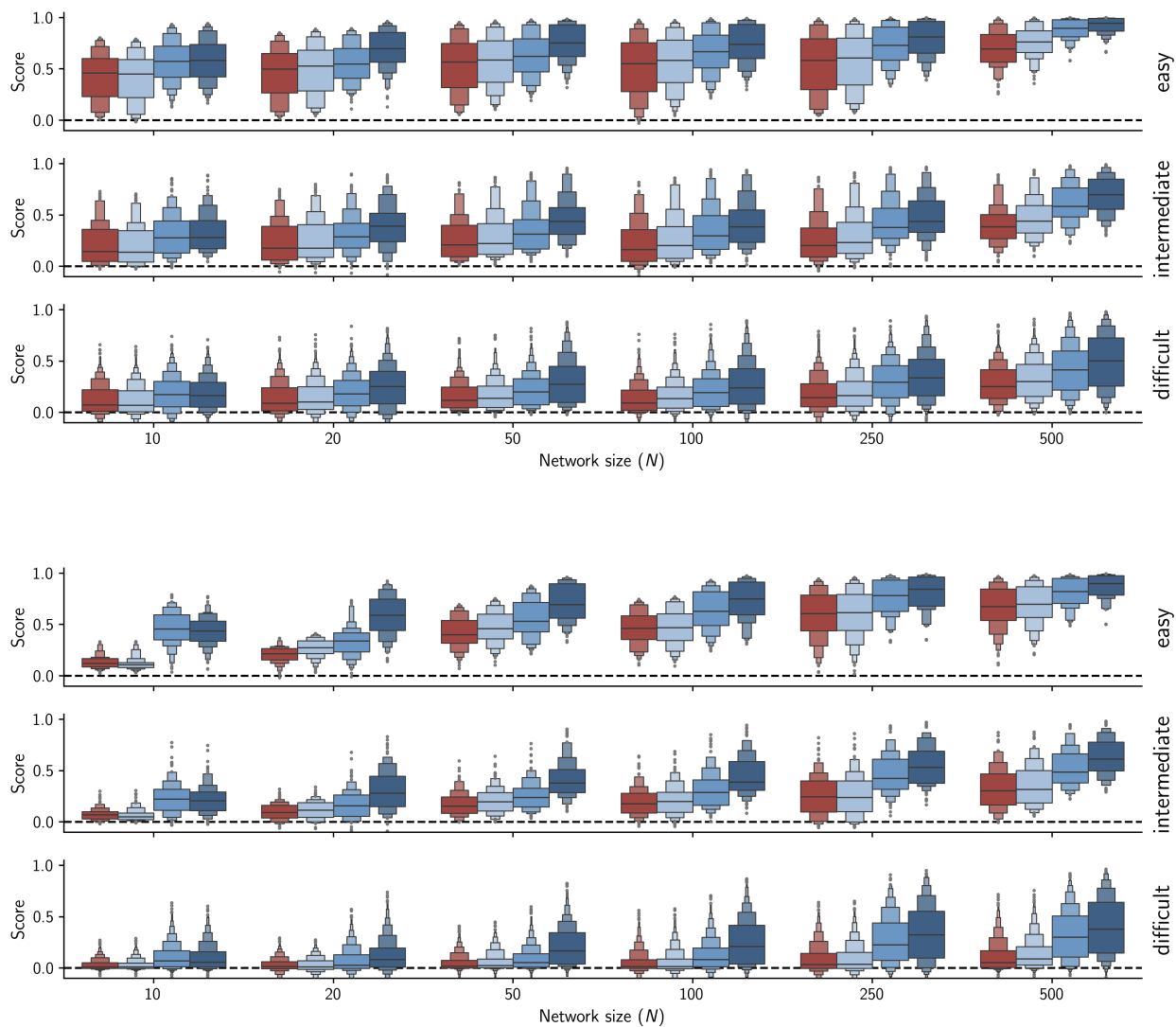
F Score distribution


Figure S.10: Variation of score distribution with network size. Performance distributions for (top) rate-based and (bottom) spiking networks across (rows) tasks of different complexities. The mean of each distribution corresponds to the levels shown in Figures 3B and S.7B, respectively. The color code is the same as in the main text.

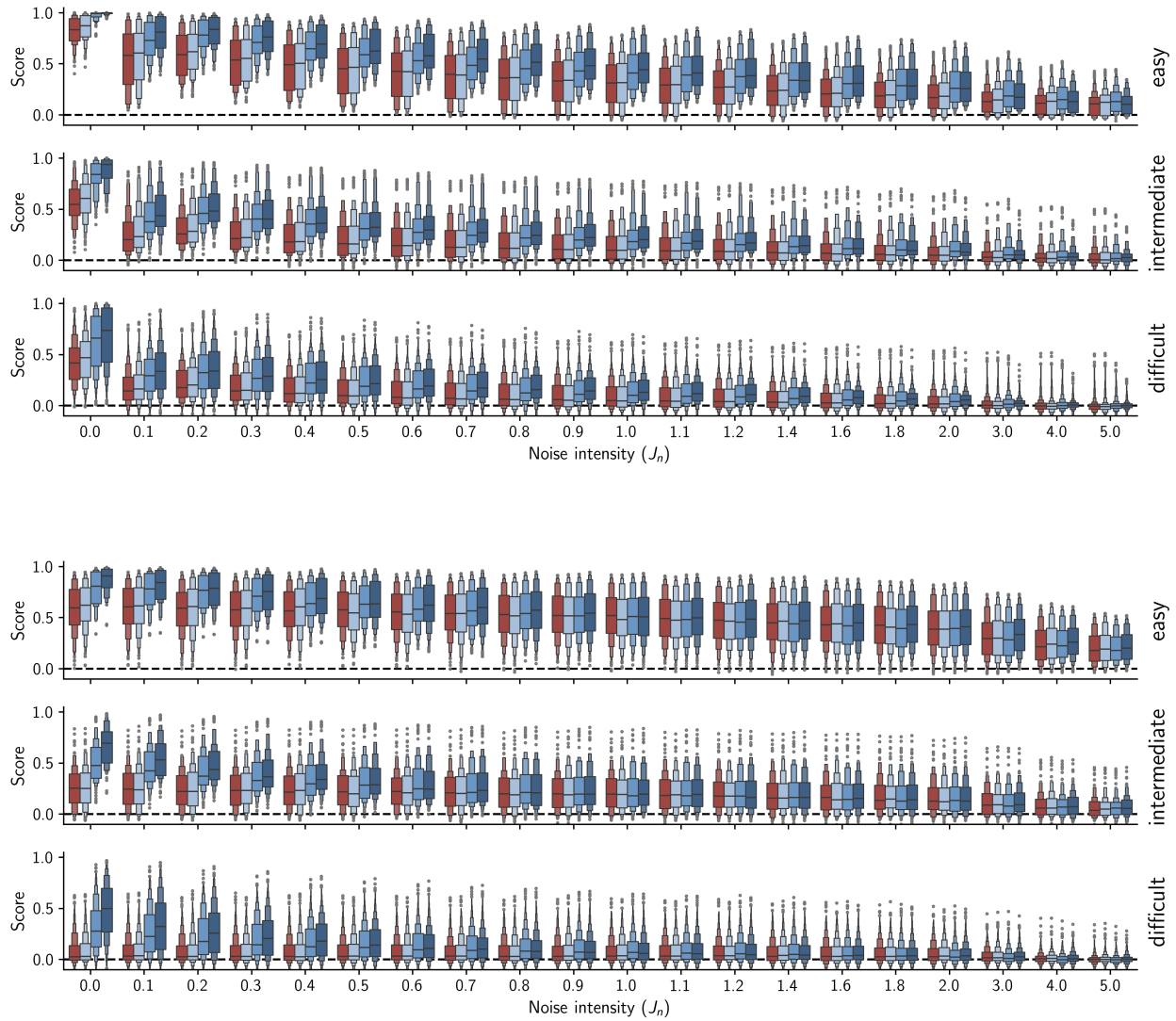


Figure S.11: Variation of score distribution versus noise intensity. Performance distributions for **(top)** rate-based networks and **(bottom)** spiking networks across **(rows)** tasks of different complexities. The mean of each distribution corresponds to the levels shown in Figures 3C and S.7C, respectively. The color code is the same as in the main text.

Skewed Neuronal Heterogeneity Enhances Efficiency On Various Computing Systems

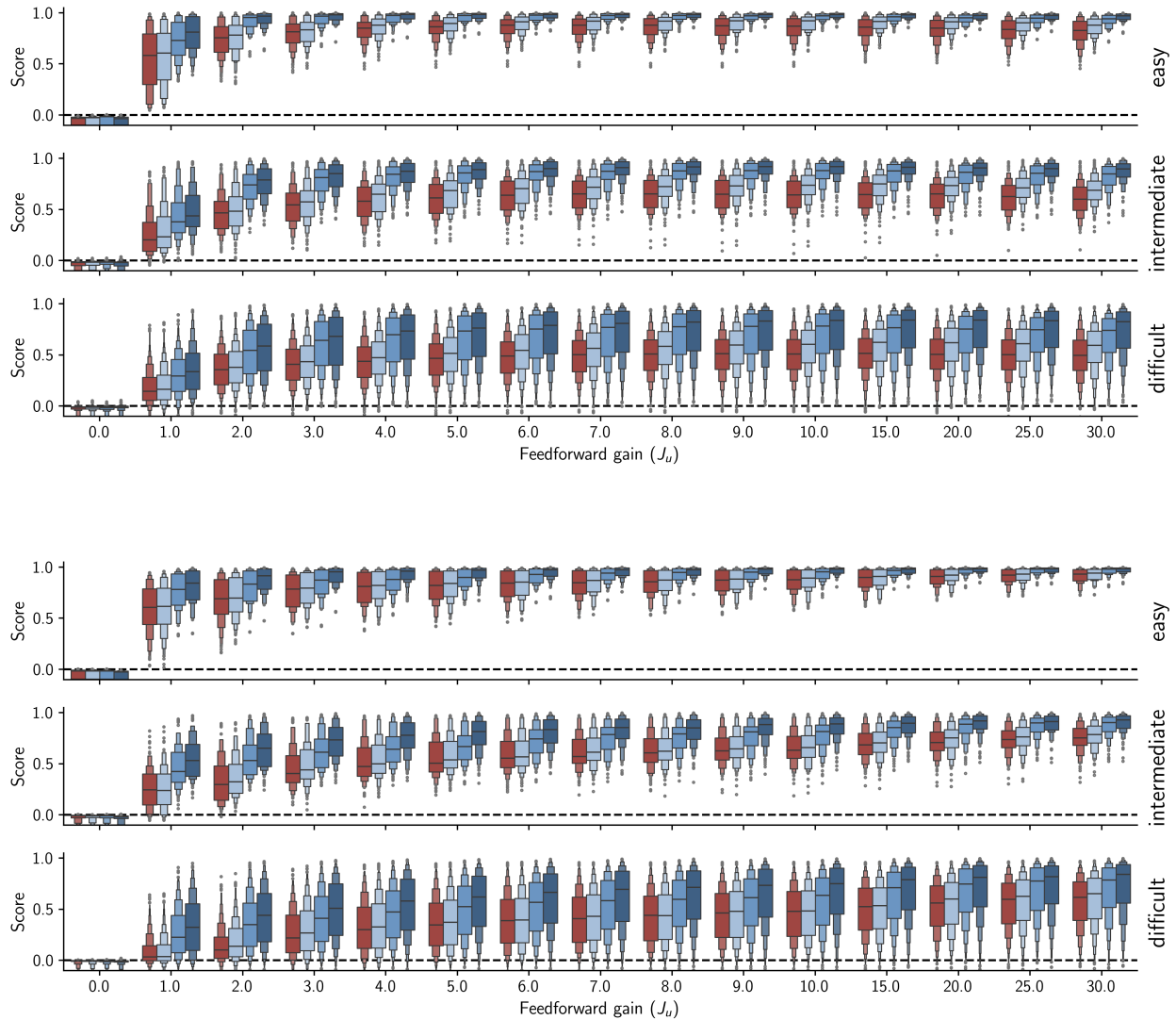


Figure S.12: Variation of score distribution versus input gain. Performance distributions for **(top)** rate-based networks and **(bottom)** spiking networks across **(rows)** tasks of different complexities. The average of each distribution corresponds to the levels shown in Figures 3D and S.7D, respectively. The color code is the same as in the main text.

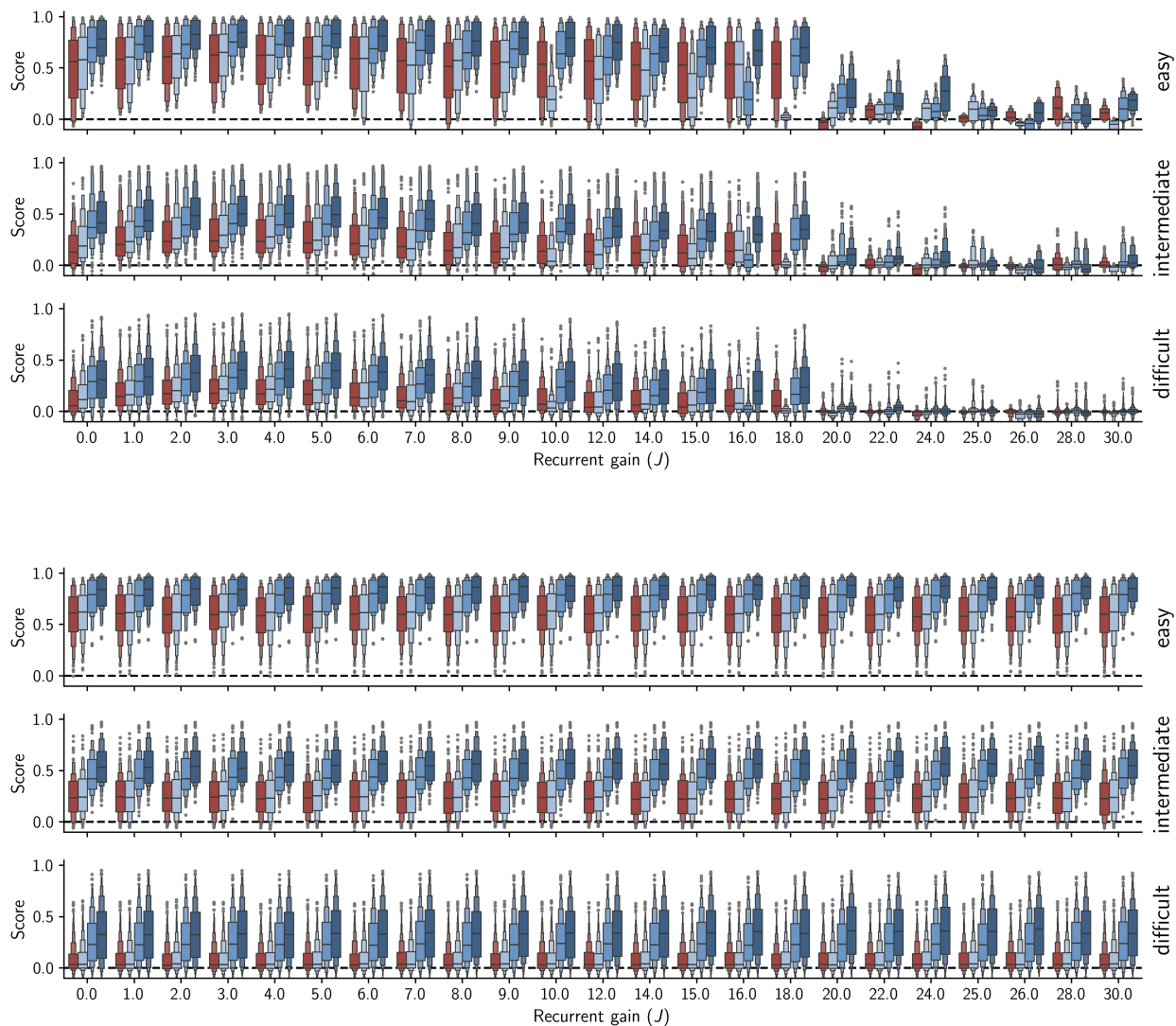


Figure S.13: Variation of score distribution versus recurrent gain. Performance distributions for **(top)** rate-based networks and **(bottom)** spiking networks across **(rows)** tasks of different complexities. The mean of each distribution corresponds to the levels shown in Figures 3E and S.7E, respectively. The color code is the same as in the main text.

Skewed Neuronal Heterogeneity Enhances Efficiency On Various Computing Systems

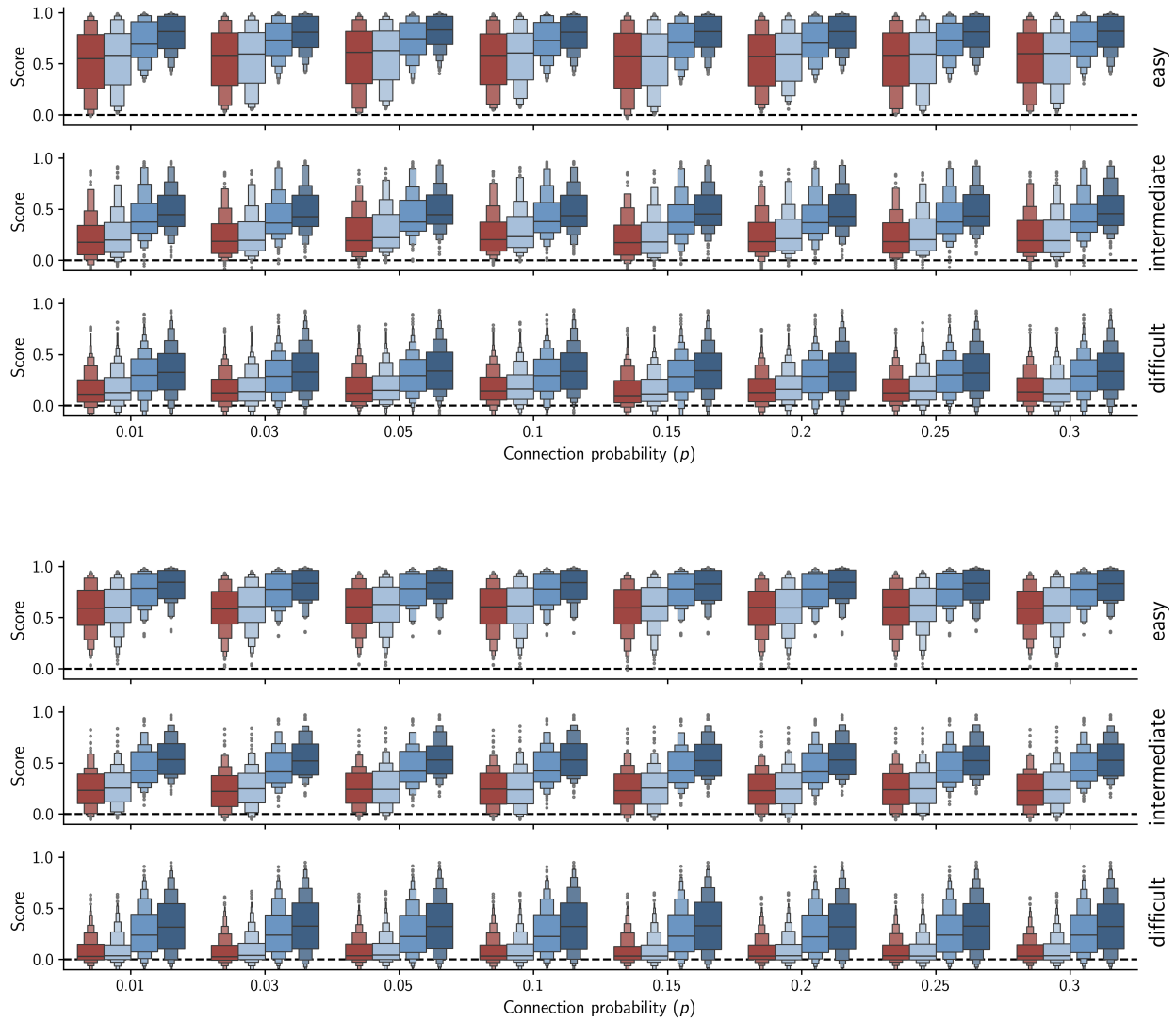


Figure S.14: Variation of score distribution versus connection probability. Performance distributions for **(top)** rate-based networks and **(bottom)** spiking networks across **(rows)** tasks of different complexities. The mean of each distribution corresponds to the levels shown in Figures S.8B and S.9B, respectively. The color code is the same as in the main text.

Skewed Neuronal Heterogeneity Enhances Efficiency On Various Computing Systems

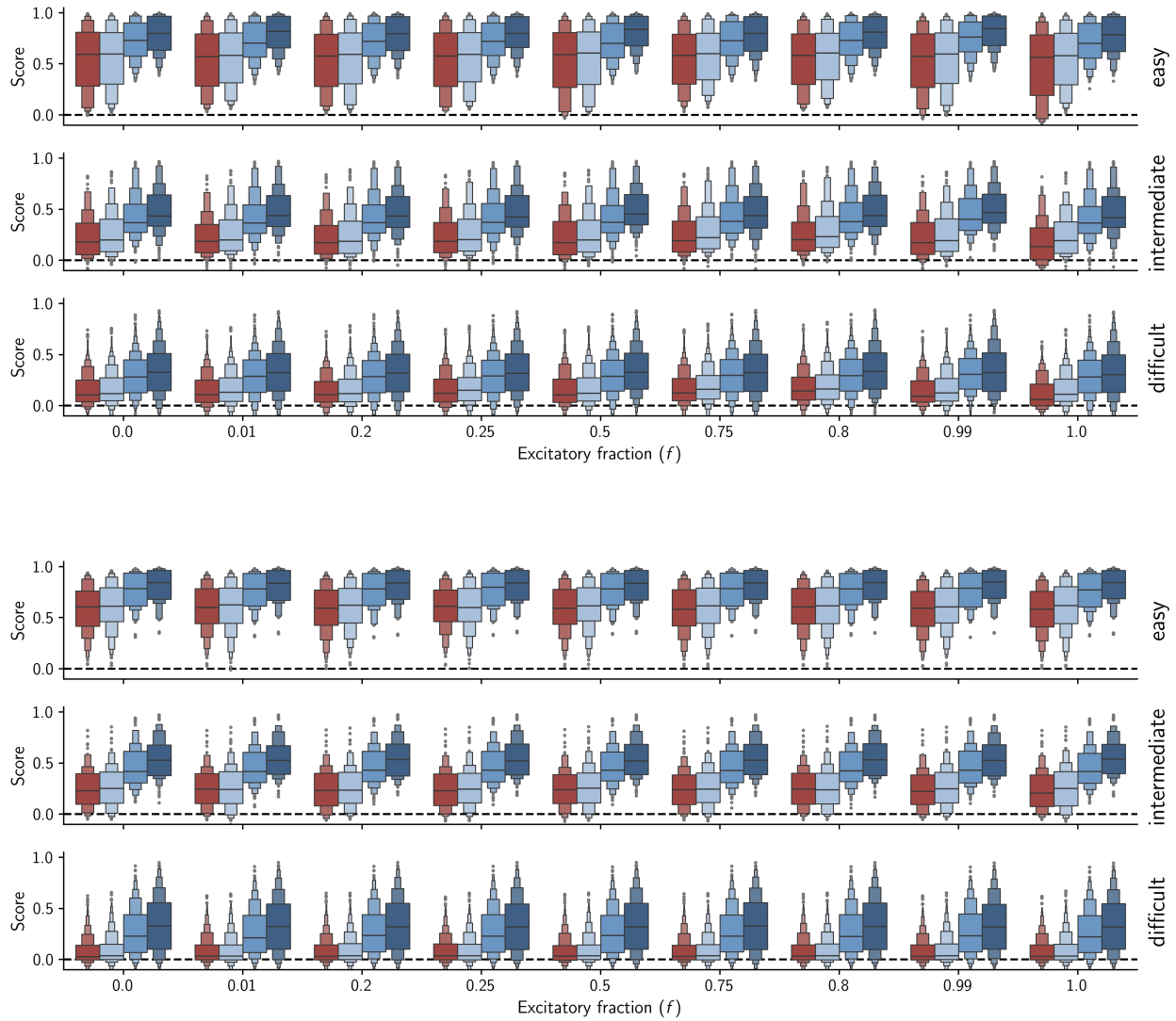


Figure S.15: Variation of score distribution versus excitation-inhibition ratio. Performance distributions for **(top)** rate-based networks and **(bottom)** spiking networks across **(rows)** tasks of different complexities. The mean of each distribution corresponds to the levels shown in Figures S.8C and S.9C, respectively. The color code is the same as in the main text.

Skewed Neuronal Heterogeneity Enhances Efficiency On Various Computing Systems

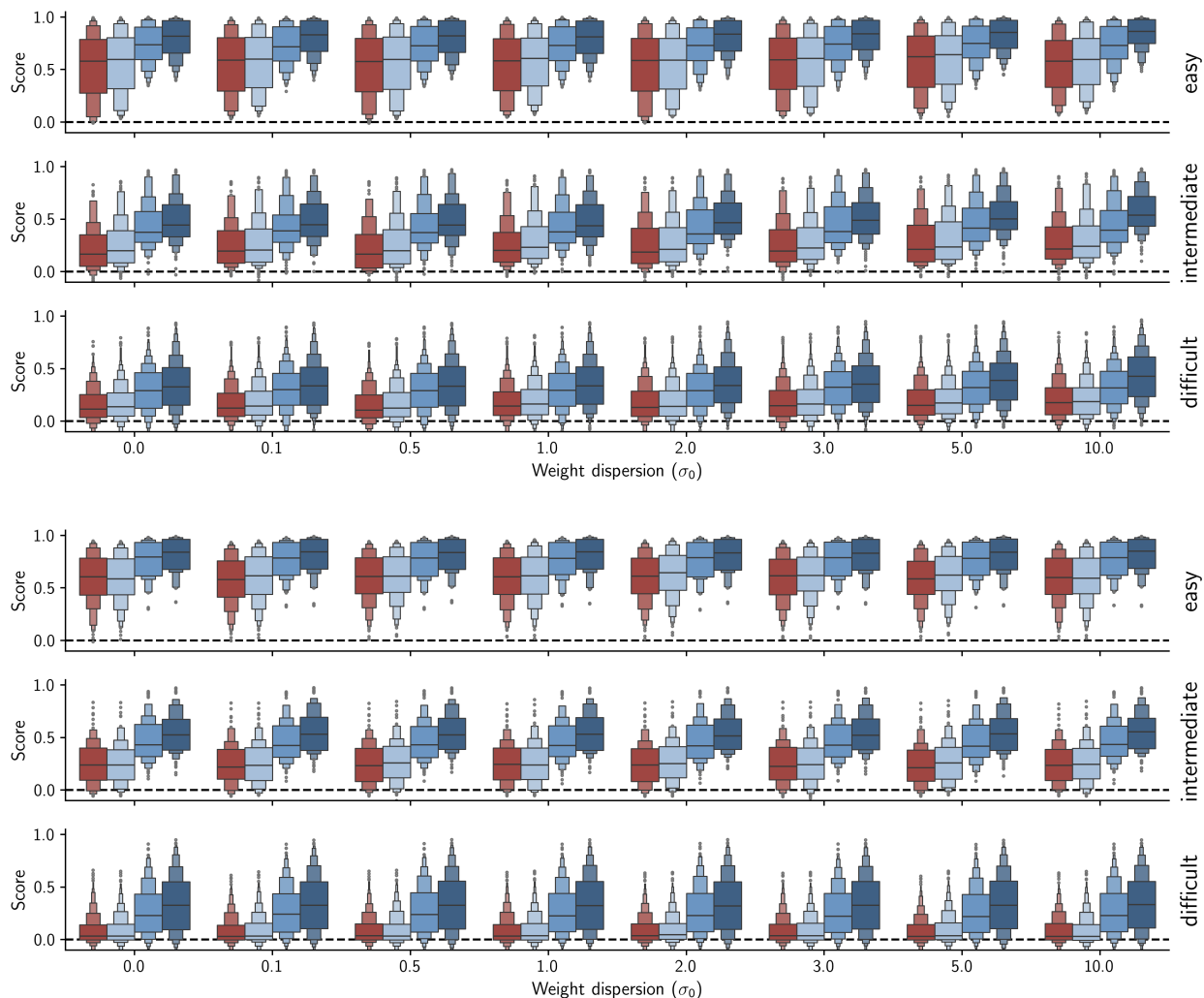


Figure S.16: Variation of score distribution versus recurrent weight dispersion. Performance distributions for **(top)** rate-based networks and **(bottom)** spiking networks across **(rows)** tasks of different complexities. The mean of each distribution corresponds to the levels shown in Figures S.8D and S.9D, respectively. The color code is the same as in the main text.

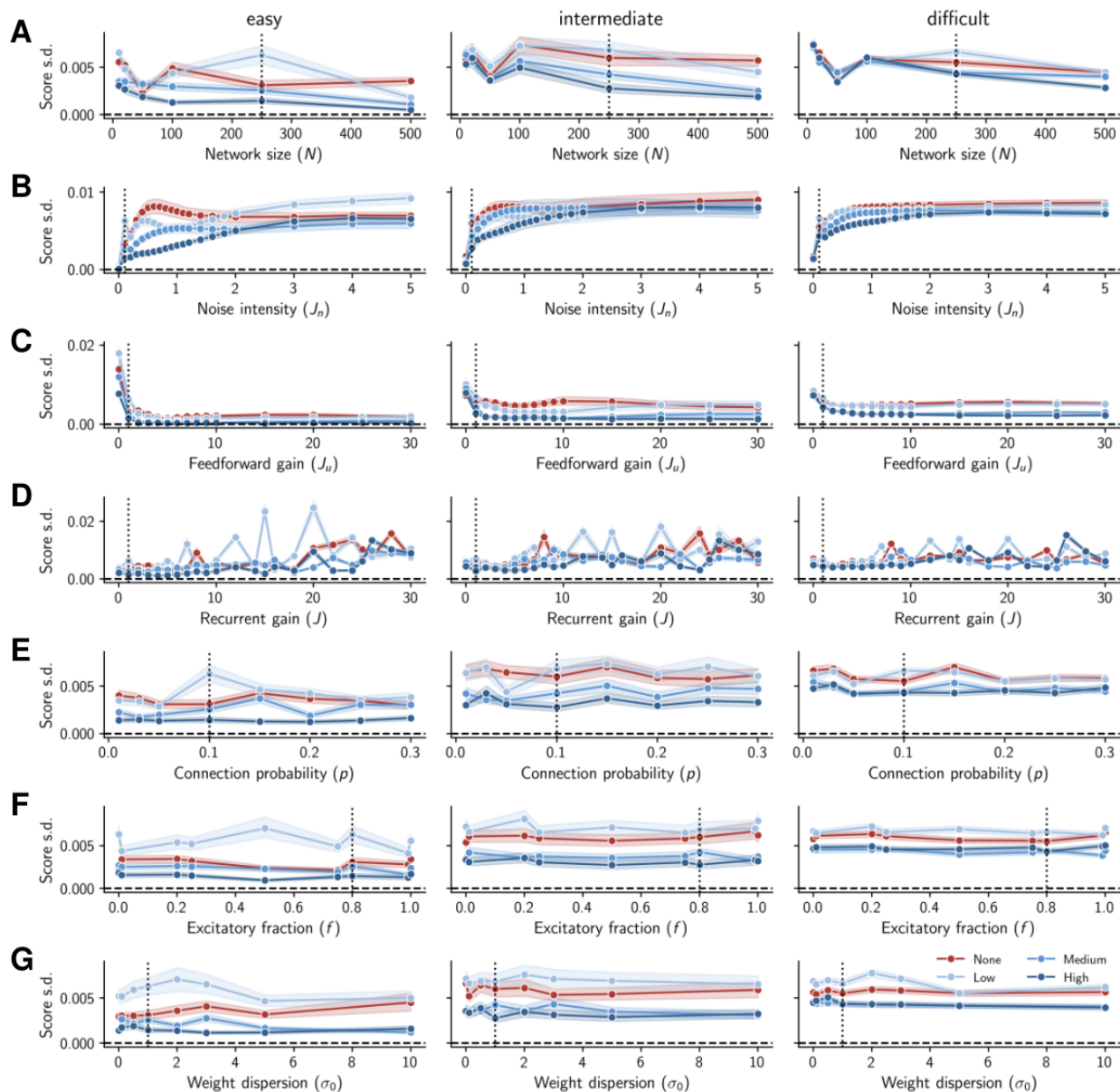
G Performance uncertainty


Figure S.17: Performance uncertainty in rate networks. Performance standard deviation of rate networks, computed from three readouts obtained with fully independent samples. The data are broken down by task-complexity tier (columns) and by the hyperparameter values shown: (A) network size, (B) noise intensity, (C) feedforward gain, (D) recurrent gain, (E) connection probability, (F) fraction of excitatory neurons, and (G) weight dispersion. The narrow range of standard deviations across all panels indicates that the error in the average performance is small, and three independent trials are sufficient. Note also the lower error observed in heterogeneous networks. The shaded areas indicate the 95% confidence interval across tasks within the corresponding complexity tier.

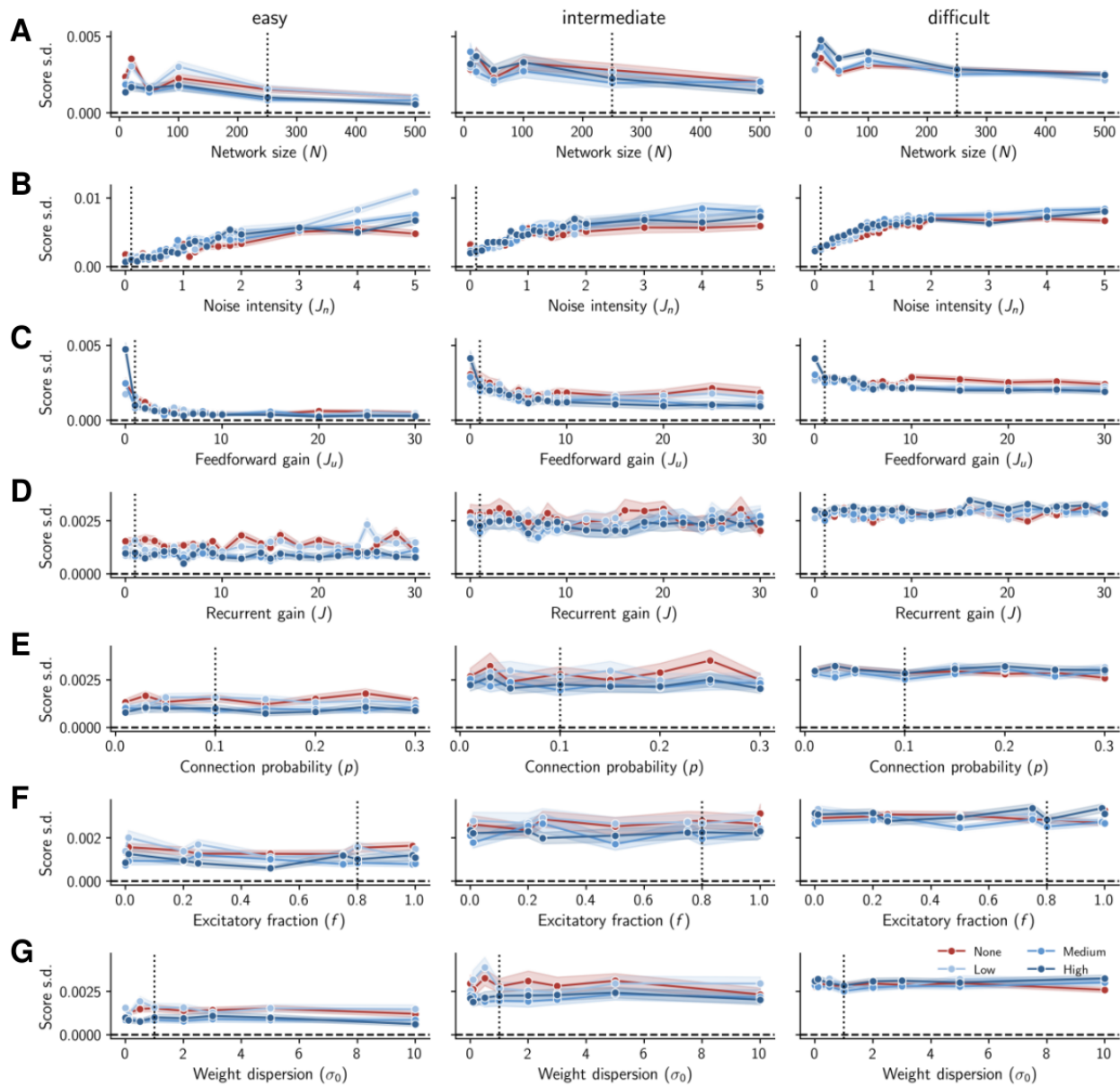


Figure S.18: Performance error in spiking networks. As in Fig. S.17, but for spiking networks. The error bars are computed from three independent readouts. As before, heterogeneous networks exhibit lower variability.

H Score and efficiency breakdown

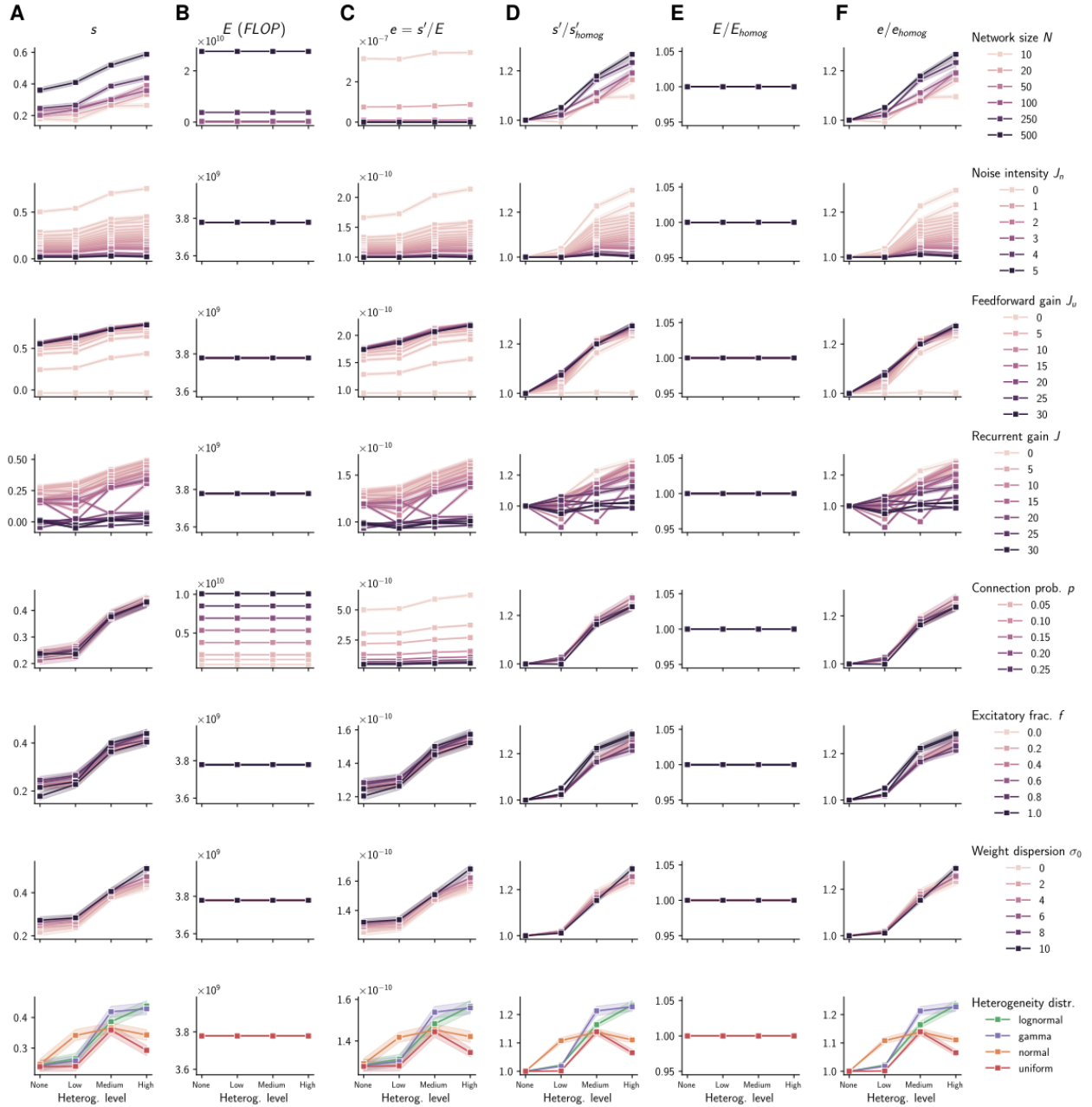


Figure S.19: Energy and performance variation of rate networks with heterogeneity. Task-averaged (A) performance s , (B) energy E , and (C) efficiency e across different heterogeneity levels, together with (D–F) their ratios relative to the corresponding values in a homogeneous network. (Rows) each varied hyperparameter. Note that, because the score $s \in (-\infty, 1]$, we first map it monotonically to the interval $(0, 1)$ via $s' = \exp(s - 1)$ before computing efficiency and the ratio metrics, thereby avoiding negative values or division by zero.

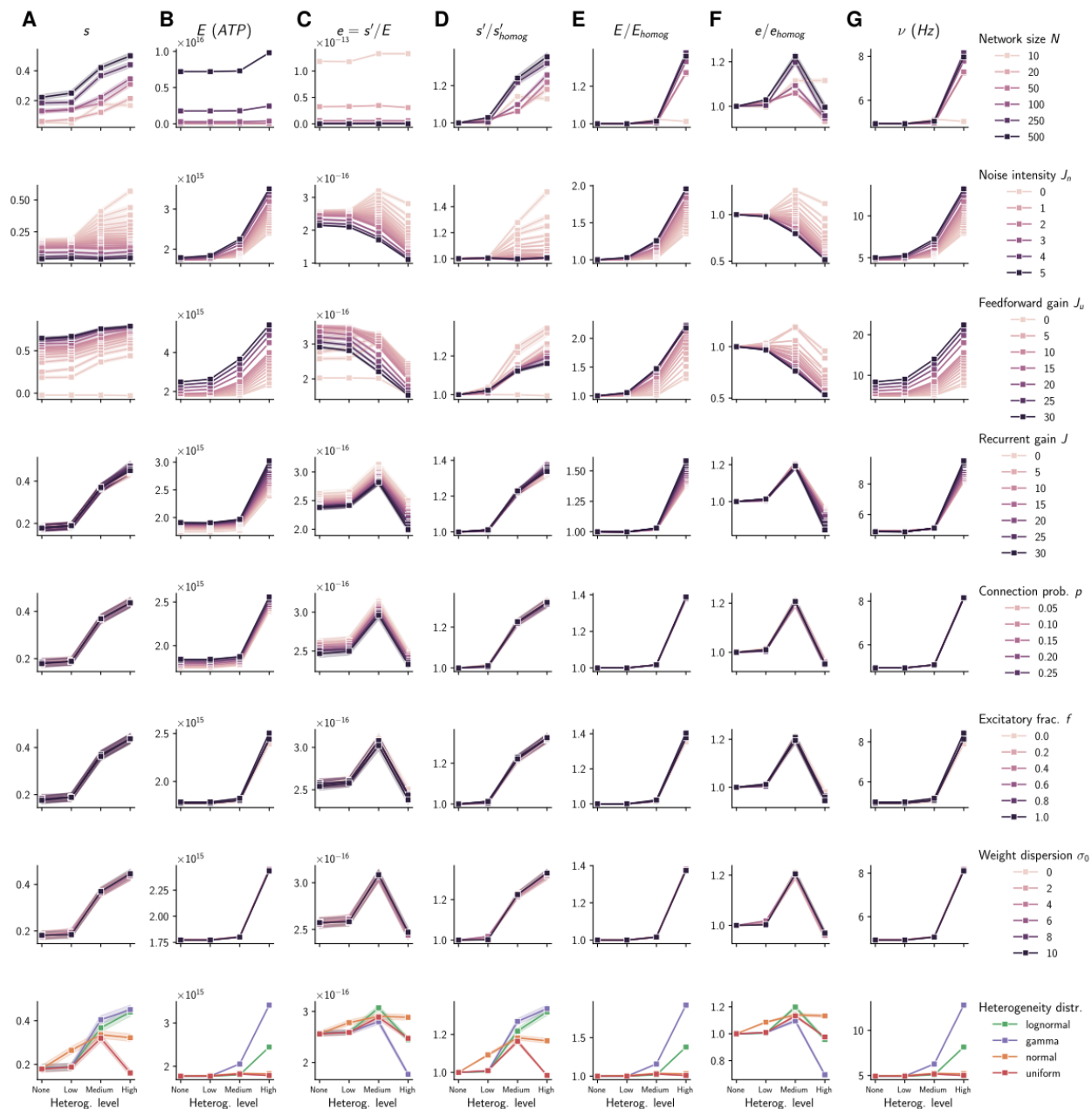


Figure S.20: Energy and performance variation of spiking networks with heterogeneity. As in Fig. S.19, but for spiking networks. (G) The additional column shows the average firing rate ν . Its correlation with E indicates that the energy increase in heterogeneous networks is primarily due to higher neuronal activity. Note that in all scenarios, the networks fire with a rate far below the maximum possible firing rate of $\nu_{\max} = 1/\tau_{\text{ref}} = 500$ Hz. Consequently, even at the maximal recurrence level simulated ($J = 30$), spiking networks stay effectively input-driven, which also explains the lack of performance variation with J in Fig. S.7E.